JMEPEG (2026) 35:4640–4660
https://doi.org/10.1007/s11665-025-11943-7

1059-9495/$19.00

ORIGINAL RESEARCH ARTICLE

Multi-scale Optimization and Computational Validation for Enhancing the Microstructure, Mechanical Properties, and Physical Performance of Wire Arc Additive Manufacturing-Fabricated SS309L Stainless Steel

S. Tamil Prabakaran, Saravanakumar Sengottaiyan, D. Yogaraj, and V.S. Shaisundaram

Submitted: 17 April 2025 / Revised: 7 June 2025 / Accepted: 21 June 2025 / Published online: 2 September 2025

SS309L stainless steel is commonly used in industries such as aerospace, marine, and energy due to its excellent resistance to high temperatures and corrosion, as well as its superior mechanical strength. This makes it an ideal candidate for fabrication using wire arc additive manufacturing (WAAM), a technology known for its high deposition rates and cost-effectiveness. However, optimizing process parameters is essential to enhance the mechanical properties, microstructure, and physical characteristics of SS309L when fabricated via WAAM. In this study, response surface methodology (RSM) was applied to optimize bead width and bead height in WAAM-fabricated SS309L. The optimization was conducted by varying welding current (100-150 A), voltage (10-20 V), and travel speed (0.1-0.3 m/min). A multi-layered wall was constructed using the optimized parameters (135 A, 16 V, and 0.1 m/min) for subsequent analysis of mechanical properties and microstructure, as well as physical examination and finite element analysis (FEA). The mechanical tests showed that the top section of the fabricated wall achieved an ultimate tensile strength (UTS) of 561.81 MPa, a yield strength of 435.63 MPa, and an elongation rate of 41.2%. The bottom section showed a UTS of 469.73 MPa with 45.6% elongation. The middle section exhibited a maximum compressive strength of 984.2 MPa. Microstructural analysis using x-ray diffraction (XRD), electron backscatter diffraction (EBSD), and scanning electron microscopy (SEM) confirmed that the top section contained fine-grained structures, while the bottom section exhibited coarser features. The porosity of the material was exceptionally low at 0.0081%. FEA simulations confirmed the experimental results, validating stress and deformation patterns. The study provides a comprehensive methodology for optimizing SS309L WAAM structures for high-performance industrial applications.

Keywords bead geometry optimization, finite element analysis (FEA), mechanical properties, microstructure, SS309L, wire arc additive manufacturing

1. Introduction

Wire arc additive manufacturing (WAAM) represents a swiftly developing metal additive manufacturing process that constructs metal components in their near-final form layer by layer through Gas Metal Arc Welding (GMAW) (Ref 1-3). WAAM has become highly popular since it achieves rapid deposition rates at affordable prices and produces sizable metal structures more effectively than traditional methods, such as PBF or DED (Ref 4-6). WAAM produces reliable results when precise control exists over welding current, combined with voltage and travel speed, because these three parameters determine both bead geometry and microstructure, as well as mechanical properties (Ref 7-9). WAAM requires the precise adjustment of input parameters to improve performance, as it determines both bead width uniformity and bead height, which helps minimize manufacturing defects and ensures mechanical consistency (Ref 10-12). GMAW-WAAM represents an excellent WAAM technique because it combines easy operation with efficient material usage and compatibility across multiple alloy types to produce stainless steel parts (Ref 13-15). The industrial applications of SS309L stainless steel include power plants, chemical processing, marine operations, and heat exchangers. The traditional manufacturing techniques for SS309L components include casting, forging, and machining processes, as they require extended periods and result in high costs (Ref 16, 17). WAAM technology for SS309L fabrication provides an appealing manufacturing solution by minimizing scrap material, enhancing operational speed, and enabling customizable product development (Ref 18, 19). The purpose of this research is to evaluate the mechanical and physical attributes of WAAM-made SS309L steel using input parameter fine-tuning to advance both structural performance and bead geometry

---

S. Tamil Prabakaran, Department of Mechanical Engineering, Government College of Engineering, Bargur, Tamil Nadu, India; **Saravanakumar Sengottaiyan**, Faculty of Engineering and Technology, Villa College, Male 20002, Maldives; **D. Yogaraj**, Department of Mechanical Engineering, Vel Tech Rangarajan Dr Sagunthala R&D Institute of Science and Technology, Chennai, Tamil Nadu 600062, India; and and **V.S. Shaisundaram**, Department of Mechanical Engineering, Vels Institute of Science, Technology and Advanced Studies, Chennai 600 117, India. Contact e-mails: sskmechanical@gmail.com and saiswastik23@gmail.com.

Graphical Abstract

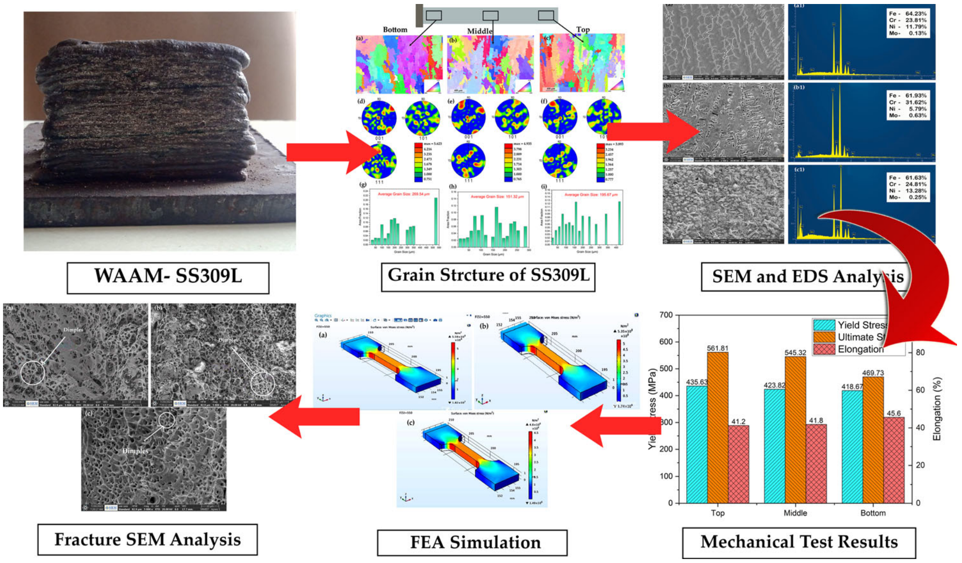

formation. The analysis conducted tensile and compression testing along with density, porosity, and microstructural examinations to analyze how the material properties change between build layers (top, middle, and bottom sections). FEA simulations serve to validate experimental data while providing insight into the implementation details, including material stress patterns and dimensional modifications. The research results will benefit WAAM technology development for the production of SS309L stainless steel components while making these products suitable for industrial sectors that require dependable, high-strength components.

Stainless steel WAAM research now focuses on achieving optimal process stage settings, as well as developing microstructural transformations and enhancing mechanical properties for superior components. According to Arunkumar et al (Ref 20), stress behaviors in WAAM-produced SS304 showed noticeable dependence on the microstructural characteristics that result from WAAM-controlled process settings. The researchers achieved accurate mechanical property predictions through a finite element analysis simulation of tensile behavior, which yielded results with an error of less than 1%. The research by Deviprasad et al (Ref 21) analyzed how a change in WAAM current values impacts bead dimensions and surface finish, along with microstructural refinement. They found that greater current strength enlarges the build zone dimensions and causes a degraded surface finish and deteriorated microstructural refinement, thus emphasizing the need for parameter optimization. Manikandan et al. (Ref 1) optimized WAAM process parameters using response surface methodology (RSM) and artificial neural networks to predict bead geometry with high accuracy (R^2 = 0.964 for BW, 0.9713 for BH). Their study identified optimal settings (135 A, 16 V, 40 cm/min), resulting in a body width (BW) of 5.8 mm and a body height (BH) of 3.65 mm. XRD, SEM, and EBSD analyses revealed significant microstructural variations and changes in grain orientation, while mechanical testing showed the highest UTS (294.11 MPa) and YS (190.38 MPa) in the bottom section. Le and Mai (Ref 22) explored the microstructural and mechanical properties of WAAM-fabricated SS308L, revealing that columnar dendrites with δ-ferrite formation within the γ-austenite matrix contribute to anisotropic properties. Tensile tests confirmed higher UTS (552.95 MPa) and elongation (54.13%) in horizontal specimens compared to vertical specimens (531.78 MPa UTS, 39.58% elongation), highlighting microstructural inhomogeneity and the need for process optimization. Shetty et al. (Ref 21) analyzed WAAM-fabricated SS310, noting elongated columnar grains with epitaxial growth and δ-ferrite formation along grain boundaries, which negatively impacted mechanical anisotropy. Their findings revealed lower ductility and yield strength in the deposition direction, as well as a 33% reduction in Charpy impact energy compared to wrought SS310, highlighting the impact of grain structure on toughness. Yang Ke and Jun Xiong (Ref 23) compared single-wire and double-wire feed Gas Tungsten Arc (GTA) additive manufacturing (SWF-AM and DWF-AM) for SS308L, concluding that DWF-AM enhances cooling rates, refines microstructures, and improves strength (571 MPa UTS versus 492 MPa in SWF-AM). The finer cellular grains in DWF-AM improved hardness (174 HV versus 118 HV in SWF-AM), enhancing mechanical performance. Chaudhari et al. (Ref 24) studied WAAM-fabricated SS309L, identifying delicate granular structures at the bottom, columnar dendrites in the middle, and coarser dendritic structures at the top. Their mechanical testing results confirmed that WAAM-fabricated SS309L achieves the desired properties. Recent studies have explored various deposition methods and optimized additive manufacturing processes using response surface methodology (RSM) (Ref 25, 26). Elaiyarasan et al (Ref 27, 28) investigated the wear behavior of coatings applied via electrospark deposition, focusing on WC-Cu composite electrodes to enhance the wear resistance of alloys such as Ti-6Al-4V. Similarly, research by Elangovan et al. (Ref 29) examined the machining of AZ31B magnesium alloys using sustainable electrical discharge machining (EDM) with B4C-enriched biodielectric fluids to improve surface integrity. Furthermore, studies on titanium alloys, such as those by Elaiyarasan et al (Ref 30), have evaluated the tribological performance of composite electrode-assisted electrical discharge machining

(EDM), confirming the improved performance of WC-Cu coatings for enhanced durability and wear resistance. These advancements underscore the importance of optimizing process parameters and utilizing innovative materials to achieve superior mechanical properties and surface finishes.

Despite significant advancements in WAAM of stainless steel, research on SS309L fabricated using WAAM remains limited, particularly concerning the systematic optimization of bead geometry and its correlation with mechanical, microstructural, and physical properties. Previous studies have primarily focused on tensile properties and microstructural analysis, without addressing comprehensive process parameter optimization to enhance deposition quality. While RSM has been successfully applied in optimizing other stainless steel grades, no prior research has utilized these techniques specifically to improve the bead geometry of SS309L. Additionally, the FEA validation of mechanical behavior in WAAM-fabricated SS309L remains unexplored, limiting the ability to establish a predictive framework for stress distribution and deformation behavior. Another significant research gap is the lack of physical property evaluations, particularly density and porosity measurements, which are crucial for ensuring the structural integrity of WAAM-produced SS309L components. Furthermore, compression testing has not been extensively explored for WAAM-fabricated SS309L, leaving a gap in understanding how WAAM-induced thermal cycles influence compressive strength and deformation characteristics.

This research aims to fill these gaps by applying RSM on bead geometry optimization, which ensures functionalized deposition characteristics without generating defects. Unlike previous studies on WAAM, which have primarily focused on experimental investigations, this research integrates FEA simulation to validate the optimized WAAM parameters. This approach enables the accurate prediction of stress–strain distribution and mechanical performance for different build sections. Furthermore, this study is the first to conduct comprehensive physical property analysis, including density and porosity measurements, on WAAM-fabricated SS309L, ensuring structural integrity and suitability for industrial applications. Additionally, the research performs the first known compression test on WAAM-fabricated SS309L, providing valuable insights into compressive strength, material deformation, and structural stability under load.

The novelty of this study lies in its multifaceted approach, integrating process optimization, mechanical testing, microstructural analysis, FEA validation, and physical property assessment. This makes it the first comprehensive study on SS309L WAAM, offering critical insights into optimizing WAAM-fabricated stainless steel components. The findings of this research have significant implications for aerospace, marine, energy, and industrial applications, where high mechanical integrity, low porosity, and optimized strength are crucial for performance and durability.

2. Materials and Methods

2.1 Materials

In the present work, the GMAW-based WAAM technique was employed to construct a wall on an SS316L substrate plate (dimensions 200 × 200 × 20 mm) using SS309L wire with a diameter of 1.2 mm. Table 1 shows the elemental makeup of the SS309L metallic wire and SS316L substrate plate.

Table 1 Chemical Composition of SS309L Wire and SS316L Substrate Plate (Ref 24, 31)

Element	SS309L wire, wt.%	SS316L substrate, wt.%
Fe	Balance	Balance
Cr	22.0-24.0	16.0-18.0
Ni	12.0-15.0	10.0-14.0
Mn	≤ 2.0	≤ 2.0
Si	≤ 1.0	≤ 1.0
C	≤ 0.08	≤ 0.03
P	≤ 0.045	≤ 0.045
S	≤ 0.03	≤ 0.03
Mo	…	2.0-3.0

2.2 Wire Arc Additive Manufacturing Process

SS309L structures were built utilizing a GMAW-WAAM technique. Precision deposition was achieved using a CNC-operated Panasonic YD-350GR3 power source coupled with a TA1400 6-axis robotic arm (Fig. 1b). Supplied at a steady flow rate of 15 liters per minute (L/min), the 99.99% pure argon shielding gas used during welding ensured a stable arc and helped to prevent oxidation (Ref 1).

2.3 Experimental Design and Input Parameters

Systematic variation in the process parameters allowed RSM to maximize bead width (BW) and bead height (BH). The selected parameters include welding current, voltage, and travel speed, as these are critical to controlling the deposition characteristics of WAAM. The ranges for these parameters were chosen based on a combination of literature studies, preliminary experiments, and the need to optimize the mechanical and microstructural properties of the WAAM-fabricated SS309L. Table 2 lists the main input parameters and their respective ranges (Ref 32).

Based on the Design of Experiments (DOE) methodology (Ref 33, 34), twenty-seven trial runs were conducted. During each run, single weld beads of approximately 140 mm in length were deposited, as depicted in Fig. 1(b). Using a digital caliper, bead width (BW) and bead height (BH) were measured three times within the stable area of each weld bead, and the average results are compiled in Table 3. These variations in parameters were designed to capture the effects of each on the bead geometry and to optimize the deposition characteristics without generating defects.

2.4 Multi-Layer Wall Fabrication

Multi-layer walls were constructed using the chosen values, following the identification of the ideal parameters from the single-pass experiments. The walls consisted of ten layers (Fig. 2), laid out in an alternating pattern to minimize distortion and ensure consistent heat distribution. Between layers, a 40-second cooling time was used to help appropriate heat drainage. The distance between the contact tip of the welding torch and the workpiece was kept constant at 12 mm throughout the fabrication process.

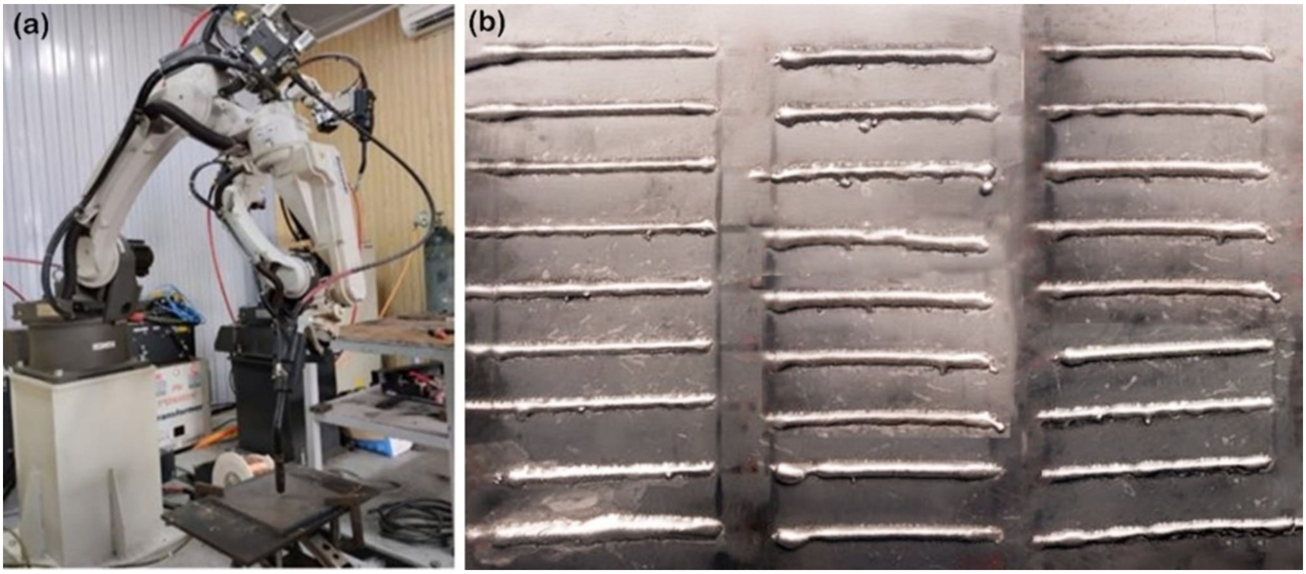

Fig 1 (a) WAAM Equipment (b) Single weld

Table 2 Different Levels of Input Parameters

Input parameters	Level 1	Level 2	Level 3
Current, A	100	125	150
Voltage, V	10	15	20
Travel speed, m/min	0.1	0.2	0.3

2.5 Mechanical and Microstructure Characterization

The fabricated material is further machined to meet ASTM criteria, physically and microstructurally defining the produced material. ASTM criteria for mechanical and microstructural characterization guided the machining of the created material. Tensile test specimen preparation followed ASTM E8, and compression test specimen preparation followed ASTM E9. To

Table 3 The bead width and bead height measurements

Experiment number	Current, A	Voltage, V	Travel speed, m/min	BW, mm	BH, mm
1.	100	10	0.1	3.61	3.18
2.	100	10	0.2	3.11	2.91
3.	100	10	0.3	2.74	2.41
4.	100	15	0.1	4.21	2.96
5.	100	15	0.2	3.93	2.65
6.	100	15	0.3	3.81	2.18
7.	100	20	0.1	4.85	2.67
8.	100	20	0.2	4.54	2.24
9.	100	20	0.3	4.22	1.95
10.	125	10	0.1	4.56	4.21
11.	125	10	0.2	4.15	3.95
12.	125	10	0.3	3.65	3.52
13.	125	15	0.1	5.18	3.92
14.	125	15	0.2	4.84	3.56
15.	125	15	0.3	4.75	3.25
16.	125	20	0.1	6.12	3.61
17.	125	20	0.2	5.65	3.15
18.	125	20	0.3	5.43	2.91
19.	150	10	0.1	4.03	3.65
20.	150	10	0.2	3.56	3.28
21.	150	10	0.3	3.12	2.95
22.	150	15	0.1	4.68	3.54
23.	150	15	0.2	4.33	3.22
24.	150	15	0.3	4.21	2.76
25.	150	20	0.1	5.48	3.22
26.	150	20	0.2	5.12	2.75
27.	150	20	0.3	4.85	2.45

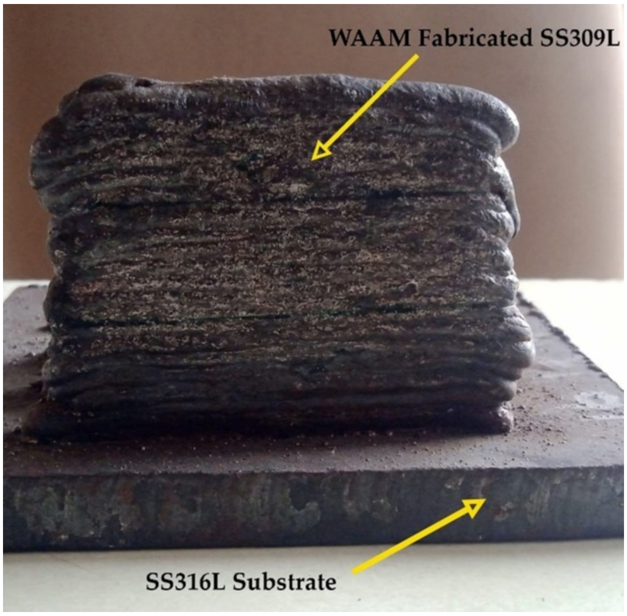

Fig 2 WAAM-fabricated wall

acquire a mirror surface, first, samples were polished using abrasive sheets of grit levels ranging from 120 to 16,000, then fine polishing using a diamond polishing agent (2 μm particle size) (Ref 35). These were etched in 10 mL of Nitric Acid (HNO_2), 20 mL of Hydrochloric Acid (HCl), and 30 mL of distilled water for 60 seconds to expose the microstructure of the specimens. (Ref 36).

2.6 Physical Characteristics

The Archimedes apparatus consists of a weighing machine and a workpiece holding mechanism. Initially, the samples 10 mm × 10 mm × 2 mm were cleaned using a sonication technique. Those samples were submerged in acetone and then set in a sonicating device for fifteen minutes. Every sample had mass noted on two separate media: air and water. Equation (1) and (2) allowed density and porosity to be computed from these measured values (Ref 37):

$$\text{Densit } (\rho_e) = \frac{(W_a * \rho_w) - (W_w * \rho_a)}{(W_a - W_w)} \qquad \text{(Eq 1)}$$

$$\text{Porosity} = \frac{(\rho_{th}) - (\rho_e)}{(\rho_{th}) - (\rho_a)} \times 100\% \qquad \text{(Eq 2)}$$

where W_a—the weight of the specimen in air, W_w—the weight of the specimen in water, ρ_w—density of water (1 g/cm^3), ρ_a—density of air (0.001225 g/cm^3), ρ_e—Density of Sample.

2.7 Numerical Analysis of Mechanical Properties

The mechanical behavior of the WAAM-fabricated SS309L was examined using FEA in COMSOL 5.6. Boundary conditions were defined by fixing one side of the model, which was designed using AutoCAD 2024 and imported into COMSOL for simulation (Ref 38, 39). A uniform force was then applied to the opposite side to replicate real-world loading conditions. The model was divided into three independent regions (top, middle, and bottom) to capture the material property variations across the structure. Material properties such as Young's modulus (193 GPa), Poisson's ratio (0.3), and density values were integrated into the simulation based on experimental measurements. Specifically, the density values were 7.65 g/cm^3 for the top section, 7.83 g/cm^3 for the middle section, and 8.45 g/cm^3 for the bottom section. These properties were critical for accurately predicting the stress–strain response, deformation characteristics, and overall mechanical performance of the WAAM-constructed SS309L under tensile and compressive loading.

2.8 Response Surface Methodology (RSM) for Bead Geometry Optimization

RSM is a statistical and mathematical method used to establish relationships between multiple input variables and response variables, revealing optimal processing conditions (Ref 40-42). The design process was then performed using Design Expert 13 software, utilizing the Optimal Design (User-defined) model (Ref 43). With this model, experimental points are allowed to be flexible, but data collection and analysis are efficient (Ref 44-46). RSM was used to develop a predictive model by systematically varying the input process parameters, current, voltage, and travel speed, based on which the optimal deposition conditions were determined (Ref 47). The approach improved predictions of bead geometry accuracy and also provided valuable insights into enhancing WAAM process stability and mechanical performance.

3. Result and Discussion

3.1 Optimization of Process Parameters to Enhance the Bead Geometry

3.1.1 Design of Experiment for WAAM Process Parameters. RSM was used to structure the DOE with an Optimal Design (User-Defined) model in Design Expert 13 software (Ref 48-50). Current (A), voltage (V), and travel speed (m/min) varied at three levels, which are the key input parameters considered for the WAAM-fabricated SS309L structures. A total of 27 experimental runs involved the deposition and characterization of single weld beads in terms of BW and BH. The experimental trials aimed to systematically evaluate the relationship between process parameters and weld bead geometry, thereby developing an empirical model to predict and optimize bead characteristics. In Table 3, all 27 experiments are tabulated, including measurements of bead width and height from the trials, as well as the results these trials yielded.

3.1.2 Analysis of Variance (ANOVA) for BW and BH. The ANOVA table (Table 4) for BW illustrates the statistical significance of the developed response model in predicting variations in BW based on WAAM input parameters. The F-value (187.39) and p value (< 0.0001) confirm that the model is highly significant. Among the individual process parameters, voltage (B) has the highest contribution of 60%, followed by travel speed (C) at 11% and current (A) at 6%, indicating that voltage is the most influential factor affecting bead width. The quadratic term A^2 (current squared) also has a significant contribution of 22%, signifying that the nonlinear effect of current impacts the bead width. Interaction terms AB

Table 4 ANOVA for BW and BH

ANOVA for BW								**ANOVA for BH**							
Source	**Sum of squares**	**df**	**Mean Square**	**F-value**	**p value**		**Contribution%**	**Source**	**Sum of squares**	**df**	**Mean square**	**F-value**	**p value**		**Contribution %**
Model	17.37	9	1.93	187.39	< 0.0001	Significant		**Model**	8.31	9	0.9237	192.66	< 0.0001	Significant	
A-Current	1.06	1	1.06	102.53	< 0.0001	Significant	**6%**	A-Current	1.21	1	1.21	252.7	< 0.0001	Significant	**15%**
B-Voltage	10.47	1	10.47	1016.71	< 0.0001	Significant	**60%**	B-Voltage	1.45	1	1.45	302.56	< 0.0001	Significant	**17%**
C-Travel Speed	1.96	1	1.96	190.3	< 0.0001	Significant	**11%**	C-Travel Speed	2.41	1	2.41	501.67	< 0.0001	Significant	**29%**
AB	0.029	1	0.029	2.82	0.1116		**0%**	AB	0.0027	1	0.0027	0.5631	0.4633		**0%**
AC	0.001	1	0.001	0.0979	0.7582		**0%**	AC	0	1	0	0.007	0.9345		**0%**
BC	0.0456	1	0.0456	4.43	0.0505		**0%**	BC	0.0001	1	0.0001	0.0156	0.9019		**0%**
A^2	3.77	1	3.77	365.57	< 0.0001	significant	**22%**	A^2	3.22	1	3.22	671.94	< 0.0001	significant	**39%**
B^2	0.022	1	0.022	2.14	0.1621		**0%**	B^2	0.0212	1	0.0212	4.42	0.0507		**0%**
C^2	0.02	1	0.02	1.94	0.1811		0%	C^2	0.0001	1	0.0001	0.0247	0.8769		0%
Residual	0.1751	17	0.0103					**Residual**	0.0815	17	0.0048				
Cor Total	17.55	26						**Cor Total**	8.4	26					
R^2		0.99						**R^2**		0.9903					
Adjusted R^2		0.9847						**Adjusted R^2**		0.9852					
Predicted R^2		0.9748						**Predicted R^2**		0.9755					

(current × voltage), AC (current × travel speed), and BC (voltage × travel speed) show negligible influence, as their p values are more significant than 0.05, indicating they are statistically insignificant. The model's R^2 value (0.99) suggests that the input parameters can explain 99% of the variation in BW, while the adjusted R^2 (0.9847) and predicted R^2 (0.9748) indicate the model's high accuracy in predicting BW responses. The ANOVA table for BH follows a similar trend, with the overall model being statistically significant (F-value: 192.66, p value < 0.0001). In some cases, such as with the voltage-parameter interaction (p-value = 0.071), the p value exceeds 0.05, suggesting that this factor may not significantly affect the response variable within the level of confidence used. This could be due to experimental variations, other dominant parameters influencing the response, or the complexity of the interaction. However, it is essential to consider the trends indicated by the analysis and the context of the overall experimental setup, as these results may still provide valuable insights. Among the primary parameters, travel speed (C) contributes the most (29%), followed by voltage (B) at 17% and current (A) at 15%, highlighting that travel speed plays a dominant role in determining bead height. The quadratic term A^2 (current squared) also significantly affects BH with a 39% contribution, suggesting that the current's nonlinear influence on BH is substantial. Unlike BW, where voltage has the highest effect, BH is more sensitive to variations in travel speed and current. The interaction terms AB, AC, and BC remain statistically insignificant, as indicated by their high p values (> 0.05). The model's R^2 value (0.9903), adjusted R^2 (0.9852), and predicted R^2 (0.9755) confirm its strong predictive capability, ensuring reliable estimation of bead height under different WAAM process conditions.

3.1.3 Contour Plot Analysis for Interaction Effects. The contour plots (Fig. 3**)** illustrate the interaction effects of process parameters Current (A), Voltage (V), and Travel Speed (m/min) on BW and BH in the WAAM-fabricated SS309L structure. The contour plots in Fig. 3(a) show that voltage (B) has a more pronounced effect on BW and BH compared to current (A). As the voltage increases from 10 to 18 V, the bandwidth increases due to a more significant heat input, which enhances material fluidity and allows for wider bead formation. However, BH initially increases and then decreases, indicating that excessive voltage results in excessive melting and spreading rather than height build-up. The desirability plot suggests an optimal region around 125a and 15v, where both BW and BH are balanced, resulting in stable deposition. The contour plots in Fig. 3(b) reveal that travel speed (C) has a significantly greater influence on BH than current (A). At lower travel speeds (0.1 m/min), the material deposition per unit length is higher, leading to an increase in BH. As travel speed increases, bead height decreases due to reduced material accumulation.

On the contrary, current has an impact on the BW of a bead by widening the bead surface area with increased current. It is shown in the desirability plot that for bead geometry which is more or less optimum all the three factors' target values are 52 m, 130A, and 0.2 m/min; the optimum bead geometry is thus achieved by setting moderate values of current (120-130A) and travel speed (0.2 m/min). A strong effect of voltage (B) interaction with travel speed (C) on BW and BH is shown in Fig. 3(c). Bead width increases at higher voltages and lower travel speeds, where more heat is input and a longer time is available for melting to occur. However, at higher travel speeds, BW decreases due to reduced deposition per unit length. The BH contour plot reveals that the bead height decreases with increasing travel speed, indicating that fast motion of the probe results in less material accumulation, a desirable region for stable WAAM deposition at approximately A travel speed of 14-16 V and 0.2-0.25 m/min is displayed on the desirability plot, where the balancing of BW and BH is shown to be required for good deposition. For this, contour analysis reveals that voltage is the primary parameter influencing BW. However, travel speed is responsible for the BH. Taking advantage of the nonlinear interaction effects, it is clear that proper parameter optimization is necessary to maintain uniform bead geometry, thereby eliminating dilution or fusion defects in WAAM-fabricated structures.

3.1.4 Residual and Model Validation Analysis. The residual and model validation analysis for BW demonstrates the effectiveness and reliability of the developed RSM model in predicting bead geometry for WAAM-fabricated SS309L structures (Ref 51, 52). The standard probability plot (Fig. 4a) confirms that the residuals (errors between actual and predicted values) follow a normal distribution, ensuring that the fundamental assumption of normality is met, which is crucial for statistical modeling. The residuals versus run plot (Fig. 4b) indicates that the residuals are randomly distributed around the zero line, without any discernible pattern, signifying that the model does not suffer from systematic errors or bias. The predicted versus actual plot (Fig. 4c) shows a strong correlation, with data points closely following the diagonal line, suggesting that the model provides highly accurate predictions of bead width based on the WAAM input parameters. Additionally, the histogram of the BW distribution (Fig. 4d) illustrates a symmetric spread of frequencies, reinforcing the assumption that the data are typically distributed and well-represented. Collectively, these validation plots confirm that the RSM model is statistically sound, well-fitted, and highly effective in optimizing and predicting BW variations in WAAM-fabricated SS309L structures, making it a reliable tool for process optimization.

The residual and model validation analysis for BH confirms the accuracy and reliability of the RSM model in predicting BH for WAAM-fabricated SS309L structures. The standard probability plot (Fig. 5a) shows that residuals follow a normal distribution, ensuring statistical validity. The residuals versus run plot (Fig. 5b) exhibits a random scatter around the zero line, indicating the absence of systematic errors. The predicted versus actual plot (Fig. 5c) demonstrates a strong correlation, with data points closely following the diagonal, confirming the high accuracy of the model. The histogram (Fig. 5d) further supports the normality of the data, displaying a well-balanced frequency distribution of BH values. These validations confirm that the BH model is statistically sound and practical in predicting and optimizing bead height for WAAM processing.

3.1.5 Optimization of Process Parameters for Maximizing BW and BH. The optimization of BW and BH in the WAAM-fabricated SS309L structure was conducted using RSM, achieving a high desirability of 0.953 (Fig. 6). The optimal parameter settings identified were a current of 129.569 A, a voltage of 18.6382 V, and a travel speed of 0.1 m/min. This combination ensures maximum material deposition while preventing excessive heat accumulation. The higher voltage contributes to a broader bead width by increasing energy input, leading to better fusion and spreading. At the same time, the low travel speed enhances bead height by allowing sufficient

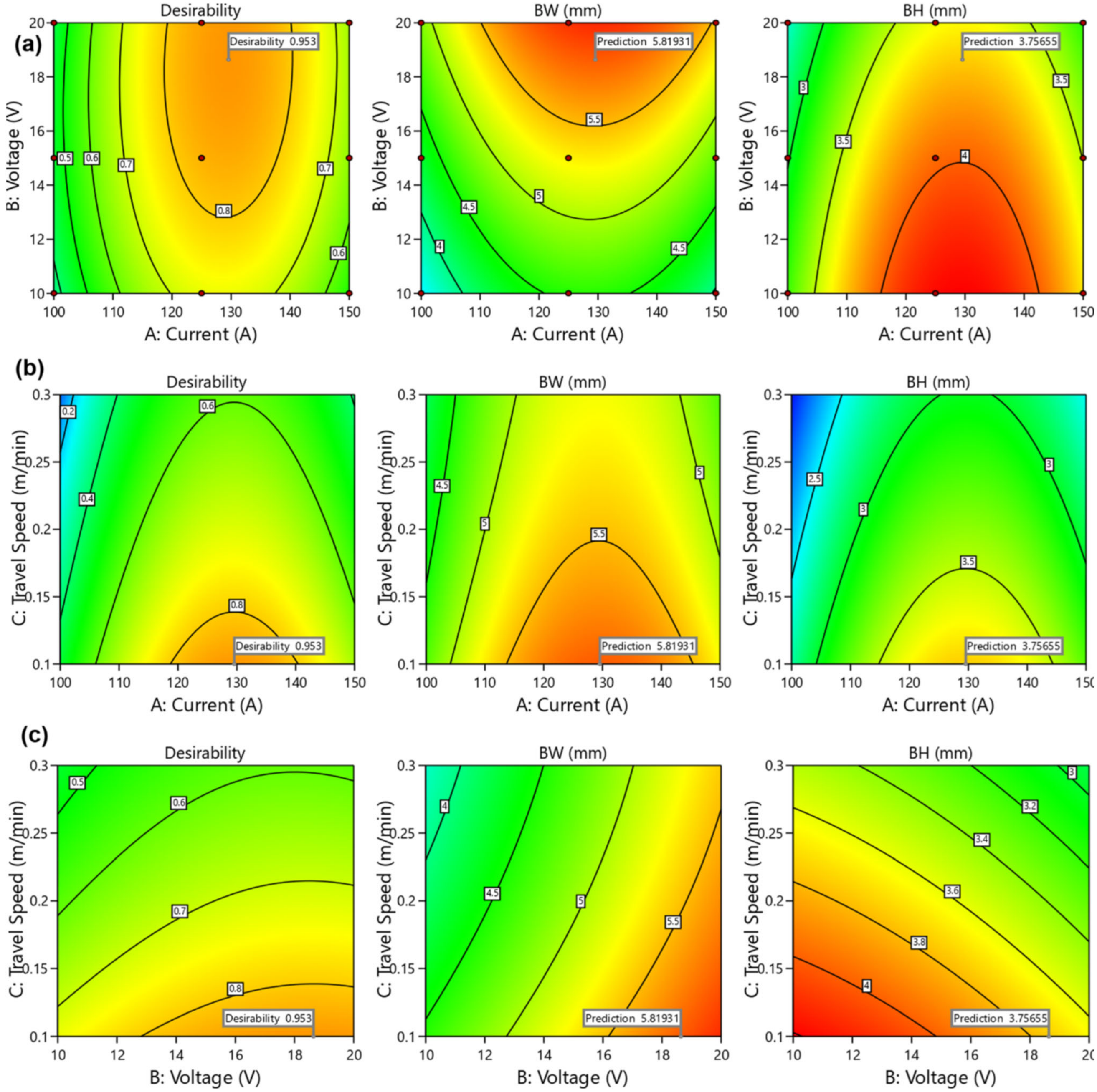

Fig 3 Contour plot analysis of interaction effects

material accumulation per unit length. The optimized results yielded a bead width of 5.81931 mm and a bead height of 3.75655 mm, confirming that the chosen parameters effectively enhance bead geometry. Finally, utilizing these optimized settings yields a well-balanced process for WAAM of SS309L and allows for uniform deposition and stable weld formation while improving the structural integrity of the fabricated components.

Having optimized these parameters, a final wall structure comprising 10 layers was fabricated to evaluate its mechanical and microstructural behavior. This multi-layer deposition ensures uniform material distribution and provides a realistic representation of WAAM-fabricated components, facilitating a thorough study of their mechanical strength and microstructural properties. The optimized settings thus provide a process with a good balance for the WAAM of SS309L, resulting in uniform deposition, stable weld formation, and enhanced structural integrity of the fabricated components.

3.2 Microstructure Analysis of the Fabricated SS309L Wall

The analysis of the microstructure of the SS309L wall fabricated by WAAM reveals significant variations in grain morphology and phase distribution across different build regions due to varying cooling rates and thermal exposure. The top section (Fig. 7a) exhibits a refined microstructure, primarily composed of austenite (γ-phase) with dispersed skeletal ferrite, a result of rapid cooling and reduced thermal accumulation. The fine grains in this region indicate a high solidification rate, which enhances hardness and tensile

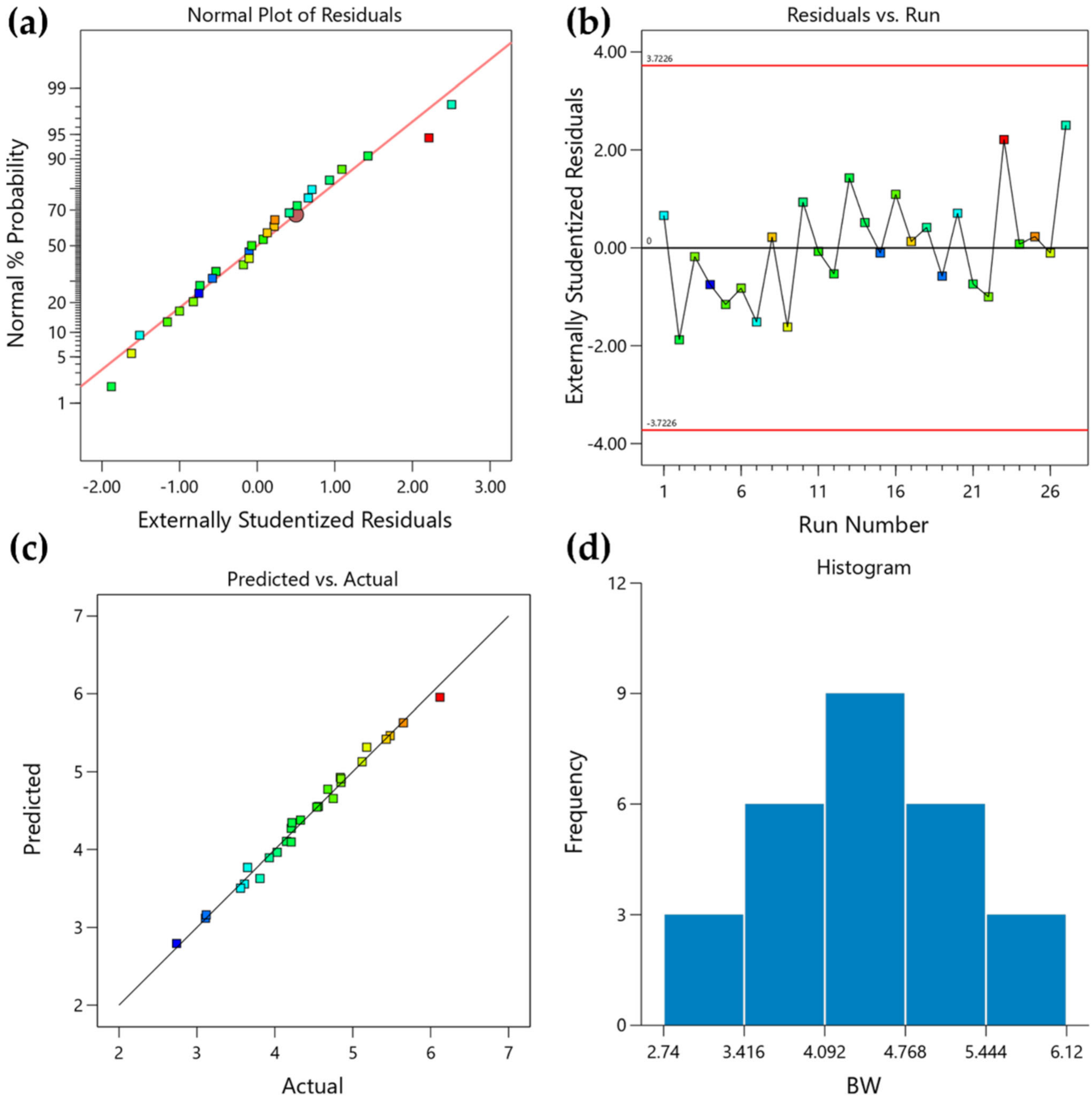

Fig 4 Residual and model validation analysis for the BW model

strength, making it suitable for high-strength applications in industries such as aerospace and energy. In contrast, the middle section (Fig. 7b) features a columnar dendritic structure with vertically aligned dendrites, indicative of a moderate thermal gradient (Ref 49). This structure, comprising a mixture of austenite and ferrite phases, provides a stable mechanical performance, striking a balance between strength and ductility. The bottom section (Fig. 7c) shows a coarser microstructure, approximately three times larger in grain size, primarily consisting of skeletal ferrite and retained austenite, due to slower cooling and prolonged thermal exposure during successive layer deposition. This coarser-grain structure leads to improved ductility and toughness, making the bottom section more suitable for applications requiring resistance to deformation, such as in components subject to high-impact or cyclic loading (Ref 53).

The XRD analysis (Fig. 7d) further supports these observations, showing characteristic peaks of austenite (γ-phase) and ferrite (δ-phase) at various crystal planes. The top region exhibits stronger austenitic peaks, indicating a higher presence of retained austenite resulting from rapid solidification. In contrast, the bottom area has a higher ferrite content, which correlates with coarser grains resulting from prolonged thermal exposure. These microstructural variations heavily influence the mechanical properties of the fabricated structure. The refined grain structure at the top enhances hardness and tensile strength, whereas the coarser grain structure at the bottom offers better ductility and toughness (Ref 54). These

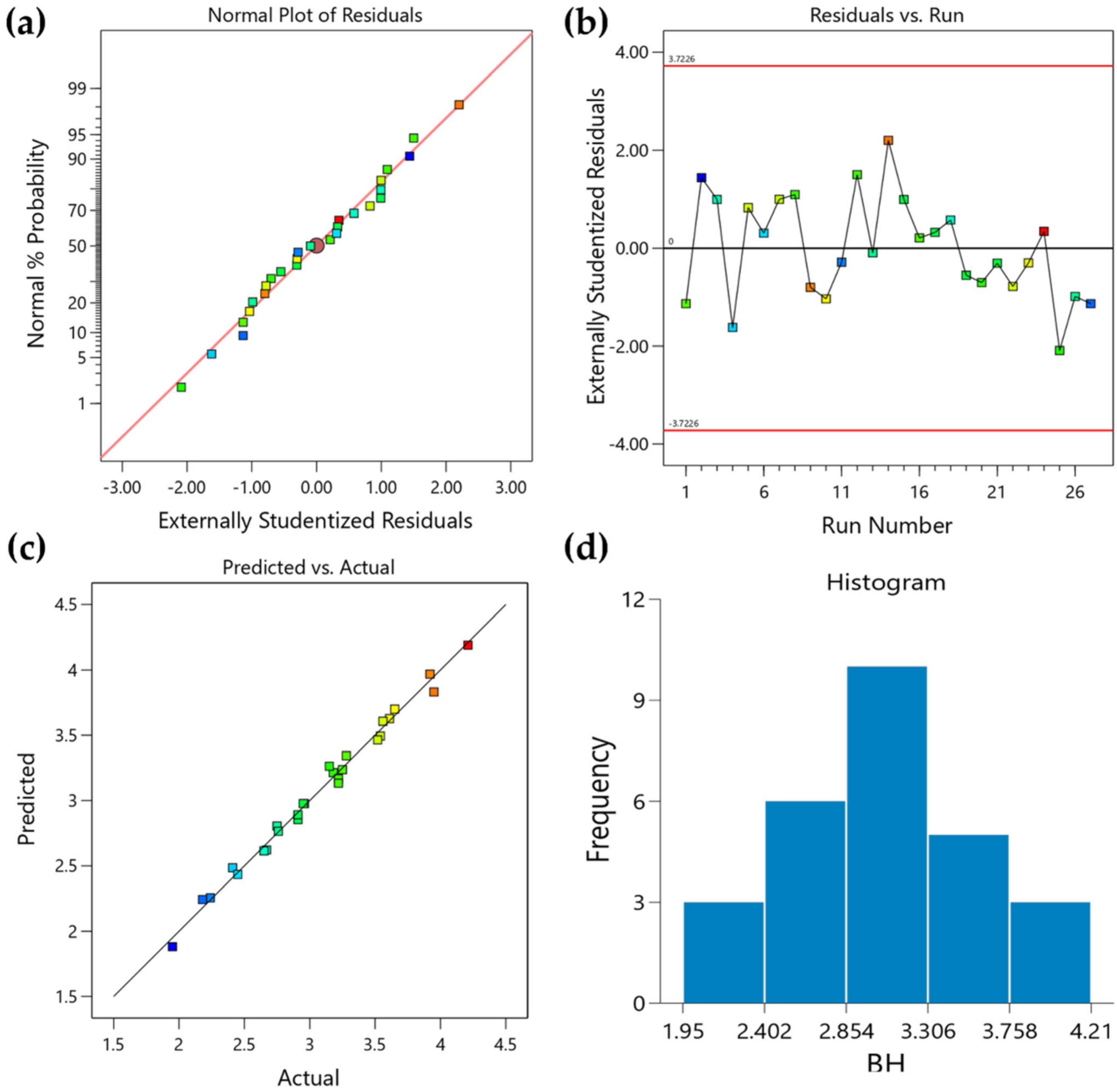

Fig 5 Residual and model validation analysis for the BH model

microstructural differences highlight the importance of controlling thermal cycles during WAAM to tailor material properties for specific industrial applications, such as high-strength components at the top and tough, deformation-resistant parts at the bottom.

3.3 The SEM and EDS Analysis

SEM and EDS analysis (Fig. 8) reveals high microstructural and compositional variations in the WAAM-fabricated SS309L structure across the top, middle, and bottom sections, resulting from differing levels of heat exposure and cooling rates during the deposition process, layer by layer. Grain morphology and phase distribution are seen on SEM images, and EDS spectra track the elemental composition of each section.

The SEM image in the top section shows a generally fine dendritic structure with well-developed cellular boundaries (see Fig. 8a). This finer microstructure is attributed to the rapid cooling rate at the surface, where heat dissipation into the surrounding environment occurs more efficiently (Ref 49). The presence of skeletal ferrite and austenite phases is visible, with a high Ni and Cr content promoting the stability of austenite. The EDS analysis (Fig. 8a1) confirms the composition, with 64.23% Fe, 23.81% Cr, and 11.79% Ni, ensuring corrosion resistance and mechanical strength. The Mo content (0.13%) is minimal, indicating reduced carbide precipitation. The middle section (Fig. 8b) presents a coarser dendritic microstructure, indicating a moderate cooling rate compared to the top region. This region experiences repeated heating and cooling cycles as new layers are deposited above it, leading to the development of both skeletal ferrite and retained austenite phases (Ref 55).

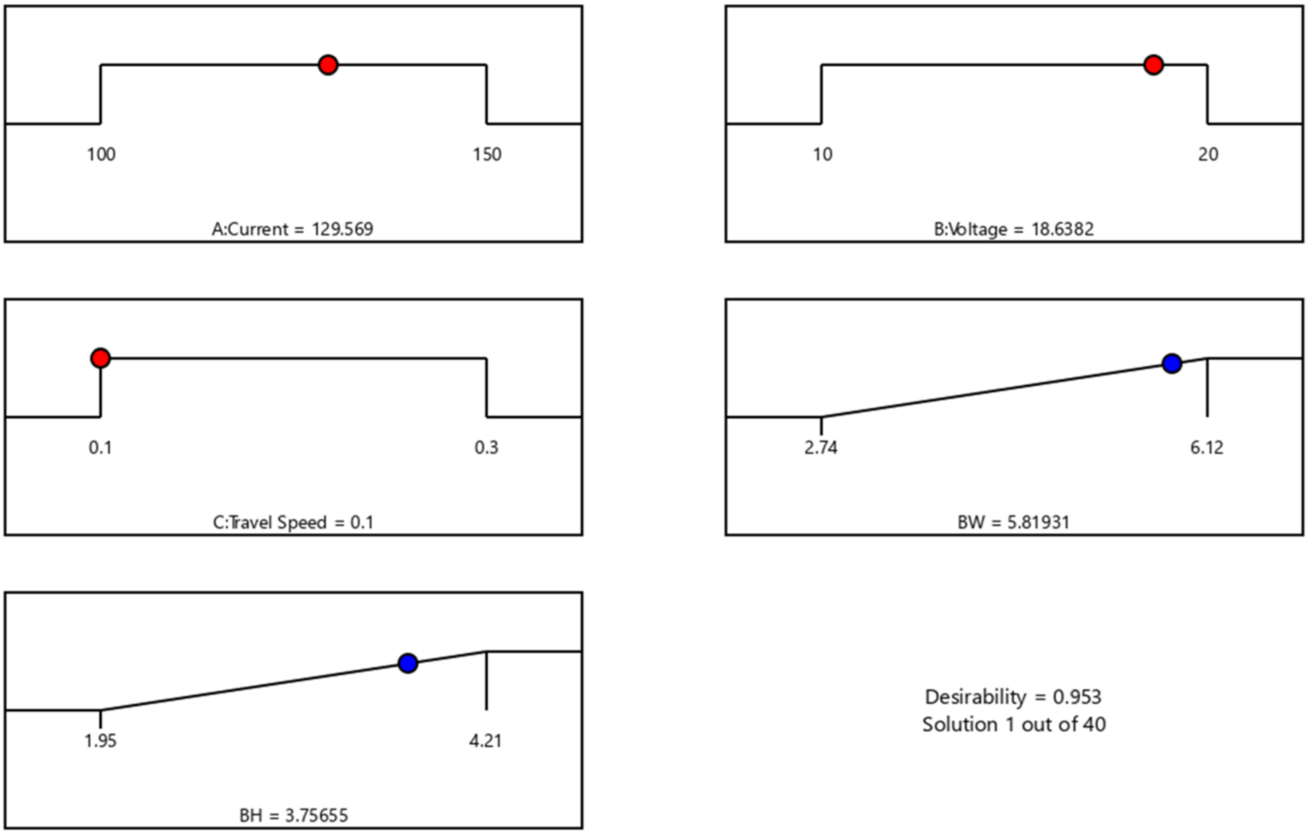

Fig 6 The optimization of BW and BH

The EDS results (Fig. 8b1) show 61.93% Fe, 31.62% Cr, and 5.79% Ni, with an increased Cr content contributing to enhanced corrosion resistance. Additionally, the Mo concentration (0.63%) is slightly higher, influencing the stability of the ferritic phase. The bottom section (Fig. 8c) shows coarsened dendritic formations and irregular grain morphology, primarily due to prolonged thermal exposure and reheating from the continuous deposition of upper layers. The grain growth in this region is more pronounced, leading to a structure dominated by ferrite with retained austenite. The EDS analysis (Fig. 8bc1) confirms that the bottom region contains 61.63% Fe, 24.81% Cr, and 13.28% Ni, with the highest Ni content, which enhances austenite stability and toughness. The Mo content (0.25%) remains moderate, contributing to localized carbide formation. Finally, it is concluded that the microstructure and composition of SS309L are influenced by the thermal cycles of WAAM (Ref 56). The top region exhibits improvement in mechanical strength due to the finer grains. Still, the bottom section, due to the coarser grains, has a lower impact on the ductility and toughness. The technology strikes a balance between phase stability and mechanical performance in the middle region. It is found that microstructural control, achieved through the optimization of WAAM parameters, is crucial for obtaining the desired mechanical properties and corrosion resistance of SS309L additive-manufactured components.

3.4 Grain Structure Analysis

A grain structure analysis of a WAAM SS309L wall was conducted from the bottom, middle, and top sections through Electron Backscatter Diffraction (EBSD) to understand grain morphology, orientation distribution, and grain size variations along the build direction. The IPF maps (Fig. 9a, b, and c) for the bottom, middle, and top sections show distinct variations in grain morphology. The bottom section exhibits coarse, equiaxed grains, indicating slower cooling rates and prolonged thermal exposure due to successive layer deposition. In contrast, the middle region exhibits a transitional grain structure, characterized by a mix of columnar and equiaxed grains, which results from intermediate cooling rates and heat accumulation from adjacent layers. The top section demonstrates fine columnar grains, formed due to rapid solidification at the surface, where heat dissipation is more efficient. The grain refinement at the top contributes to enhanced mechanical strength compared to the bottom region, where larger grains may reduce strength and increase ductility (Ref 57).

The pole figures (Fig. 9d, e, and f) provide insights into the crystallographic texture of the WAAM-deposited SS309L wall. The intensity distributions suggest variations in texture strength across different regions. The bottom section exhibits the highest texture intensity (max = 5.623), indicating a strong preferred orientation resulting from extended thermal exposure and slower cooling rates, which allowed grains to grow in specific orientations. The middle section shows a moderate texture intensity (max = 4.935), reflecting a balanced grain growth influenced by directional heat flow. The top section exhibits the lowest texture intensity (max = 3.893), confirming the presence of finer grains with a weaker preferred orientation, which is attributed to rapid cooling and inhibits grain growth in the dominant crystallographic direction.

The grain size distribution histograms (Fig. 9g, h, and i) further highlight the grain evolution along the build height. The

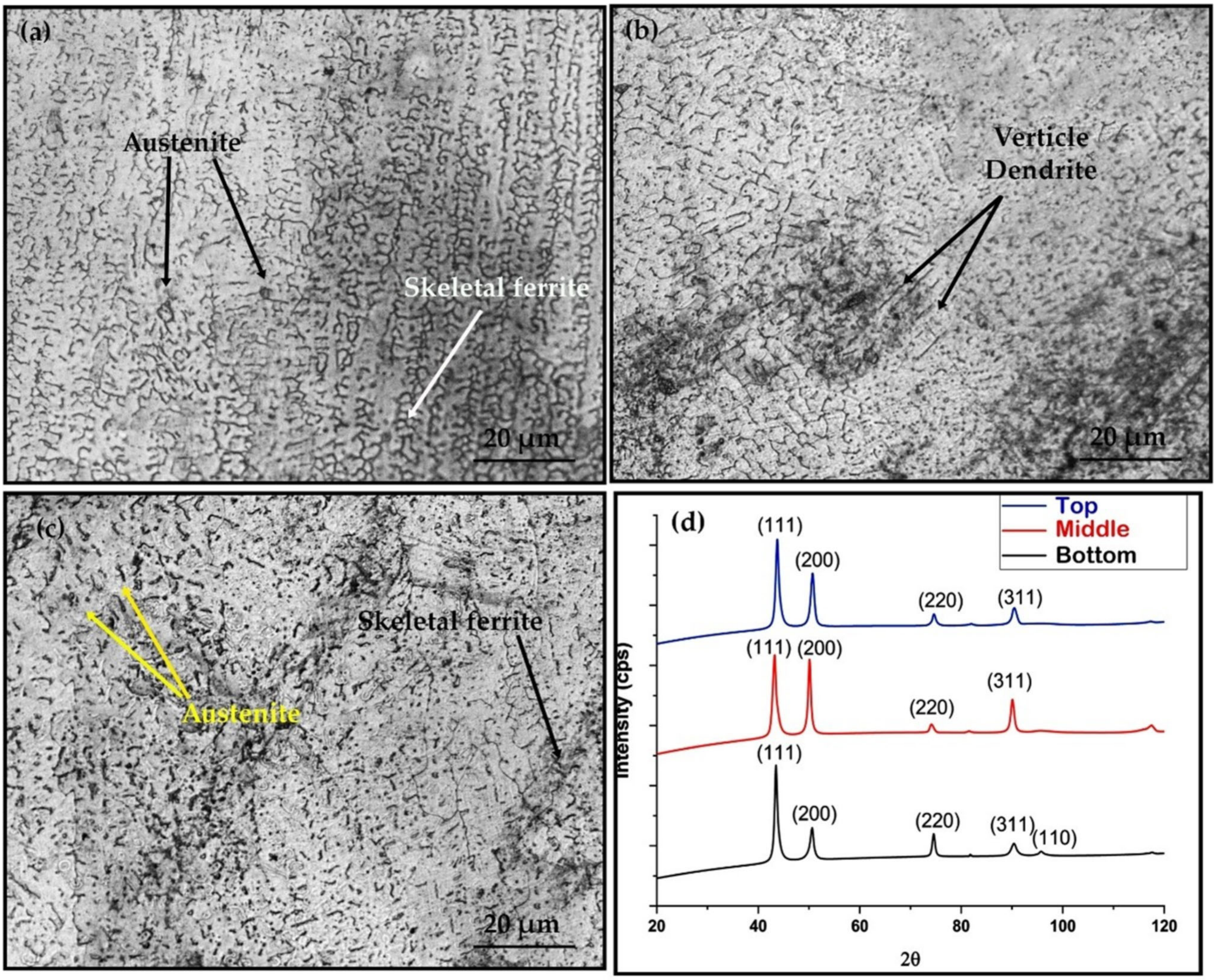

Fig 7 Microstructure analysis at (a) top (b) middle (c) bottom portion and (d) XRD analysis

bottom section has the largest average grain size (269.54 μm), indicating prolonged grain growth due to heat accumulation from continuous layer deposition. The middle section shows a reduced average grain size (151.32 μm) due to a balance between heat input and cooling rates. The top section exhibits an average grain size of 195.67 μm, which is larger than the middle section but smaller than the bottom, reinforcing the effect of rapid solidification at the final deposited layers. The histograms of grain size distribution, on the other hand, show that the middle and the top sections have a more uniform grain size distribution. In contrast, the bottom section has a wider range of grain sizes, implying non-uniform heat dissipation. Finally, the grain structure analysis verifies the considerable variation of grain morphology, texture, and size in the SS309L wall fabricated using WAAM. Strong texture orientation exists within the coarsest grains present in the bottom region, which causes ductility and lower ductility. It has a balanced microstructure in the middle section that gives an appropriate compromise between strength and toughness. It has finer grains on the top section with a weaker texture, which provides mechanical strength due to the heat rate. These findings are found to be significantly influenced by the solidification behavior as well as the thermal gradients in WAAM. They are dependent on optimum process parameters to obtain a defect-free, uniform microstructure.

3.5 Mechanical Test Analysis

3.5.1 Tensile Test Analysis. Results from the tensile test of the WAAM-fabricated SS309L wall (Fig. 10) indicate consistently high variations in the yield stress, ultimate tensile strength (UTS), and elongation at fracture between the top, middle, and bottom portions due to microstructural variation associated with thermal cycles and cooling rates during the deposition process.

In the top section, the yield stress is the highest because the grains are smaller in size. It is difficult to deform plastically; this is also because the material was rapidly cooled, resulting in finer grains. It is the middle section with a yield stress of 423.82 MPa, and finally, at the bottom, where coarser grains formed due to increased time at elevated temperature. The case with the UTS follows the same trend, with the top section having the highest UTS (561.81 MPa), the middle section (545.32 MPa), and the bottom section (469.73 MPa), which is caused by grain coarsening and increased ferrite content, resulting in a lowering of tensile strength. Although it shows an inverse trend concerning elongation (%), the bottom section,

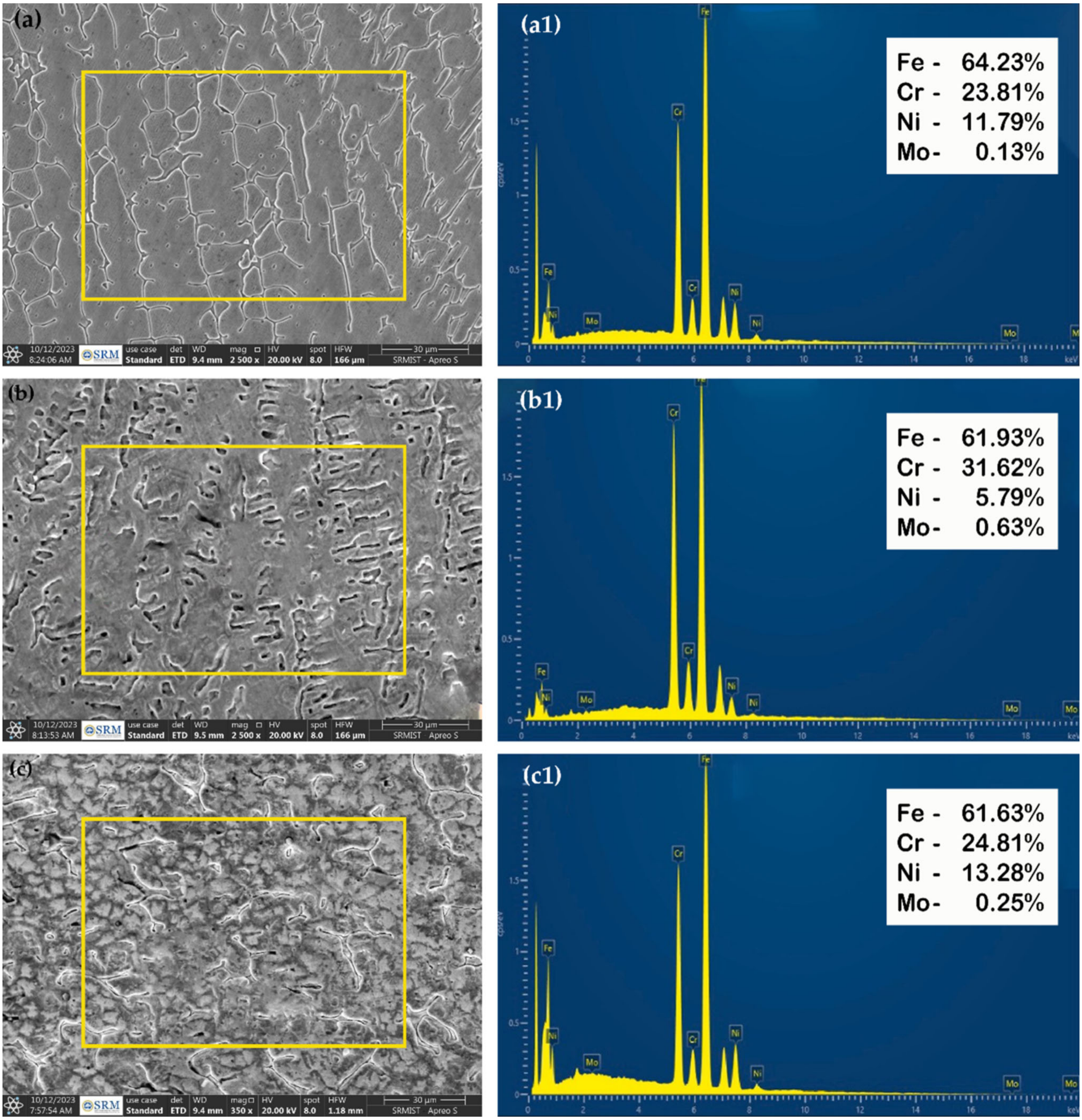

Fig 8 The SEM analysis of portion at (a) top (b) middle (c) bottom and EDS analysis (a1) top (b1) middle and (c1) bottom

which has the highest elongation (45.6%), is more ductile compared to the middle (41.8%) and top (41.2%) sections.

The stress–strain diagram of SS309L at WAAM (Fig. 11) illustrates that the material showed an increase in strength as fine grains were obtained at the top section, while showing less ductility. Black in the middle section provides high strength and ductility, while the bottom section has the highest elongation, but the lowest strength due to the coarse grains. These variations suggest the thermal effects of WAAM on the modified mechanical properties along the build direction. It implies that while the top section supports higher strength stemming from fine-grained microstructure, it is at the expense of ductility. In contrast, the bottom section has better toughness in return for smaller tensile strength. It is a suitable compromise in the area of mechanical performance because the middle section is balanced between strength and elongation. The findings show that thermal changes in the WAAM have a dramatic impact on the mechanical properties, and process optimization is a key factor in realizing the required strength, ductility, and structural integrity in stainless steel components.

The compression test findings of the WAAM-fabricated SS309L wall indicate (Fig. 12) variations in yield stress and final compressive strength among the top, middle, and bottom portions, attributable to disparities in microstructural evolution and thermal exposure throughout the additive manufacturing process. It has the highest yield stress (369.23 MPa) at the top

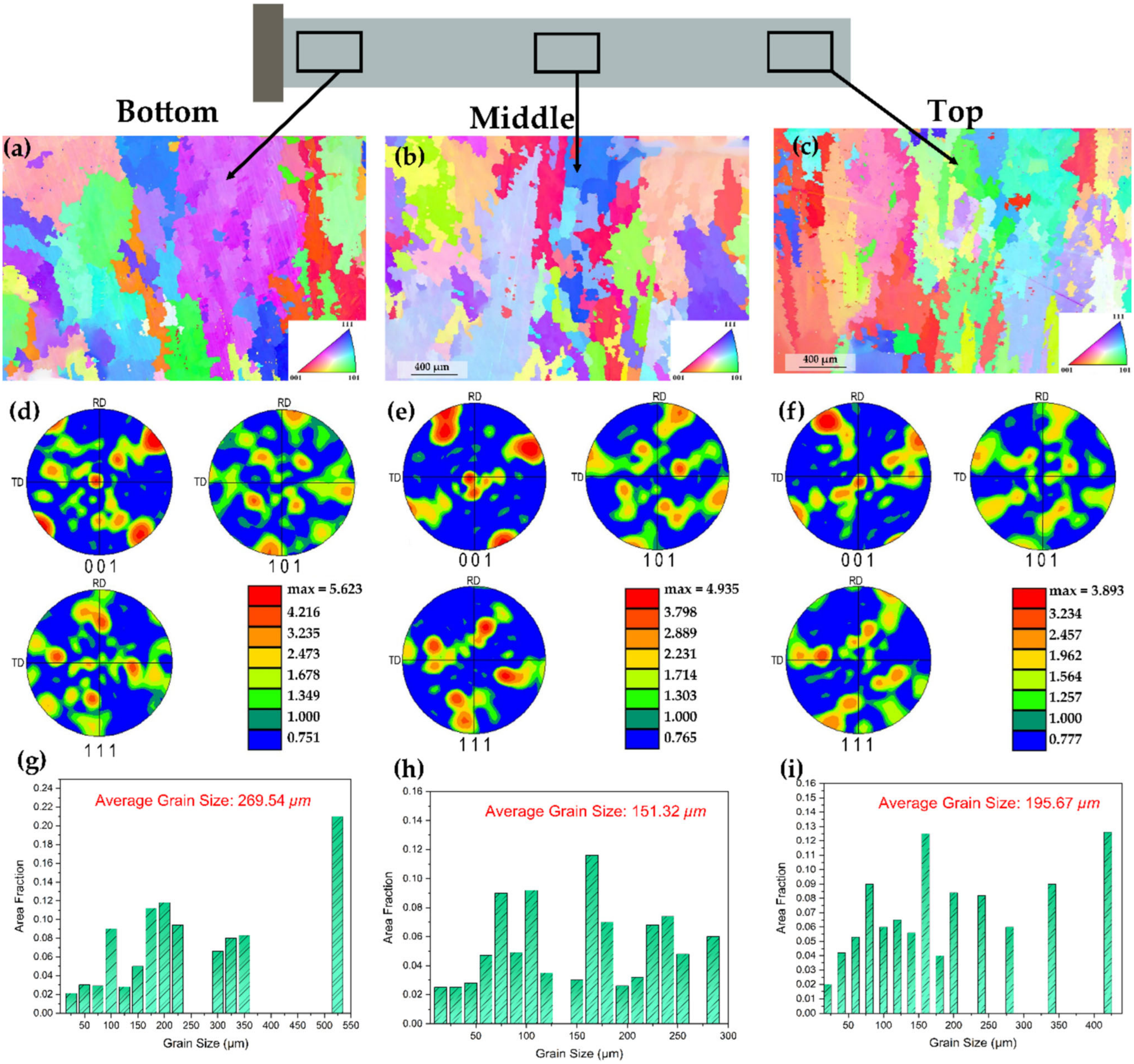

Fig 9 Grain structure analysis (a-c) inverse pole figure (IPF) maps, (d-f) pole figures, and (g-i) grain size distribution histograms

section, 358.7 MPa at the middle section, and 354.24 MPa at the bottom section. The yield stress is therefore similar to this trend; the top section property corresponds to the grain refinement at the top from rapid cooling to increase mechanical strength, while the lower section exhibits slightly less yield stress due to coarser grains formed during prolonged heat accumulation. In the same way, the ultimate stress values do not vary significantly in any of the sections, with the middle section showing the most significant stress (984.22 MPa), the top and bottom have (983.6 MPa) and (978.95 MPa), respectively. The slight variation in ultimate stress shows that the compressive load-bearing capability of the SS309L fabricated via WAAM is strong across the build direction. The middle region has a well-balanced grain structure to optimize strength and ductility. The lower ultimate stress at the bottom is attributed to higher ferrite content and larger grain structures that can decrease strength but improve deformation capacity. Overall, the results corroborate that both relevant mechanical properties of WAAM SS309L-fabricated components are excellent and are enhanced by grain refinement at the top and the middle section, where the top addition zone shows higher yield stress. In contrast, the middle section offers the best balance between strength and plastic deformation resistance.

3.5.2 FEA Simulation Analysis. The von Mises stress distribution in the WAAM-fabricated SS309L tensile specimen has been evaluated to determine the result through FEA using COMSOL Multiphysics. Under applied tensile loading, the stress concentration and deformation behavior are obtained from the simulation results. The maximum deformation occurs in the central gauge region (Fig. 13a) where the maximum stress concentration (5.59×10^8 N/m^2) is found in the top section. The high stress is in part due to the fine-grained, high-strength microstructure at which expense ductility is lost. As

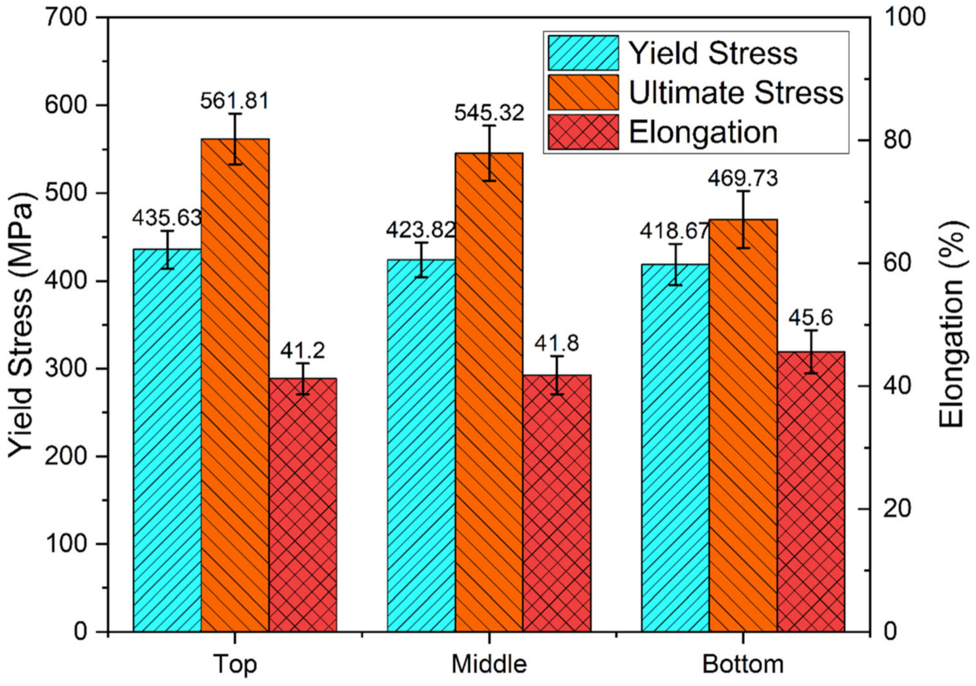

Fig 10 Tensile test results

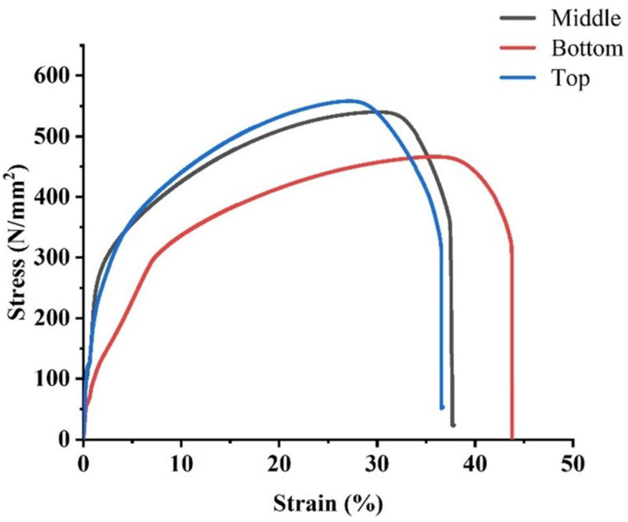

Fig 11 Stress–strain diagram for tensile test

seen in the middle section (Fig. 13b), a little less peak stress (5.35×10^8 N/m^2) is reported, which might suggest an equal state of strength versus deformation. Moderate stress distribution is obtained due to the compromise between strength and elongation, as a result of the grain structure and phase distribution in the middle region. The von Mises stress of this bottom section (Fig. 13c) (4.6×10^8 N/m^2) is also the lowest from the coarser grain structure and such a high ferrite fraction, as it does not provide hardness but does give ductility and low tensile strength. It further confirms the experimental results with the top section having the highest stress and lowest elongation, the middle section having the balanced stress and elongation, and the bottom section having the highest elongation and lowest stress. This FEA analysis is used to validate the tensile behavior of WAAM-fabricated SS 309 l and to show how thermal effects and microstructural variations affect tensile strength.

The FEA compression test simulation of WAAM-fabricated SS309L shows von Mises stress distribution under a 49,008 N load. The top section (Fig. 14a) exhibits the highest stress (9.71×10^8 N/m^2) due to its fine-grained structure, enhancing strength but limiting deformation. The middle section (Fig. 14b) has a slightly higher peak stress (9.78×10^8 N/m^2), offering a balance between strength and ductility. The bottom section (Fig. 14c) shows the lowest stress (9.6×10^8 N/m^2) due to coarser grains and higher ferrite content, improving ductility but reducing strength. The results confirm that microstructural variations in WAAM significantly impact compressive performance, with the top section providing higher strength, the middle offering stability, and the bottom enhancing deformation resistance.

3.5.3 Validation of Experiment Results with FEA Analysis. A strong correlation is shown between experimental and numerical (FEA) results for tensile and compression testing of WAAM-fabricated SS309L, therefore verifying the dependability of the FEA model. In tensile testing (Table 5), the maximum experimental stress values for the top, middle, and bottom sections were 561.81, 545.32, and 469.73 MPa, respectively. In comparison, the corresponding FEA-predicted values were 559, 535, and 460 MPa. The slight variation between experimental and numerical values (~2-3%) is attributed to microstructural heterogeneity, residual stresses, and minor imperfections in experimental conditions.

In compression testing (Table 6), the experimental maximum stress values for the top, middle, and bottom sections were 983.6, 984.2, and 978.95 MPa. In comparison, the numerical values were 971, 978, and 600 MPa, respectively. Even fewer variances (~1-2%) in the compression findings indicate that the FEA model accurately predicts the material's compressive behavior. The congruence between the experi-

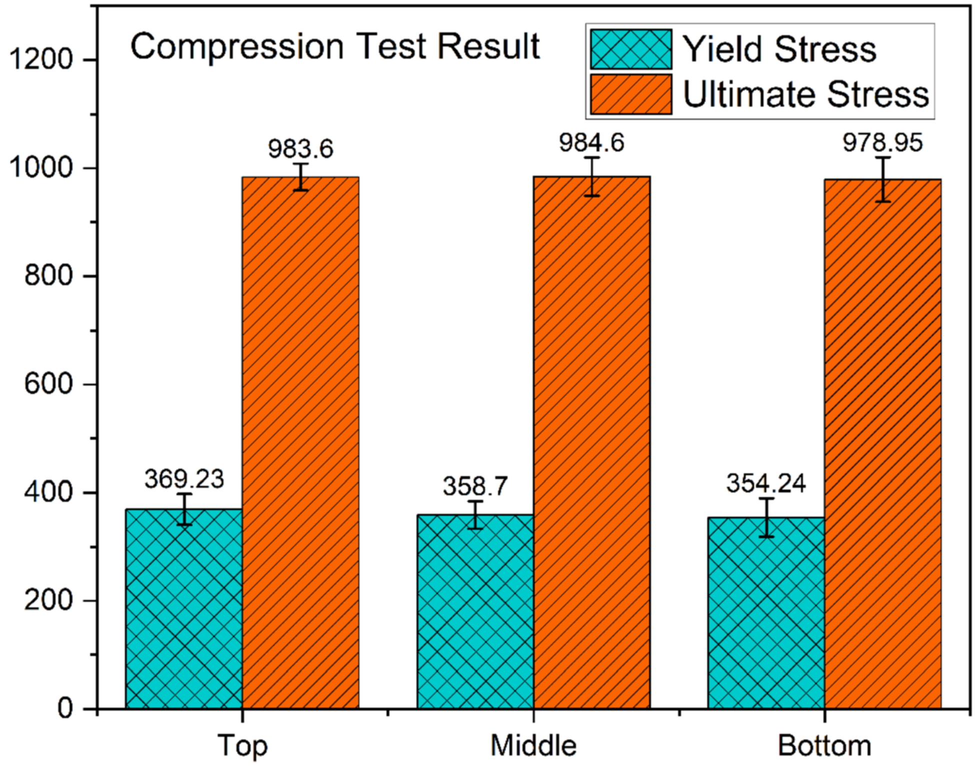

Fig 12 Compression test results

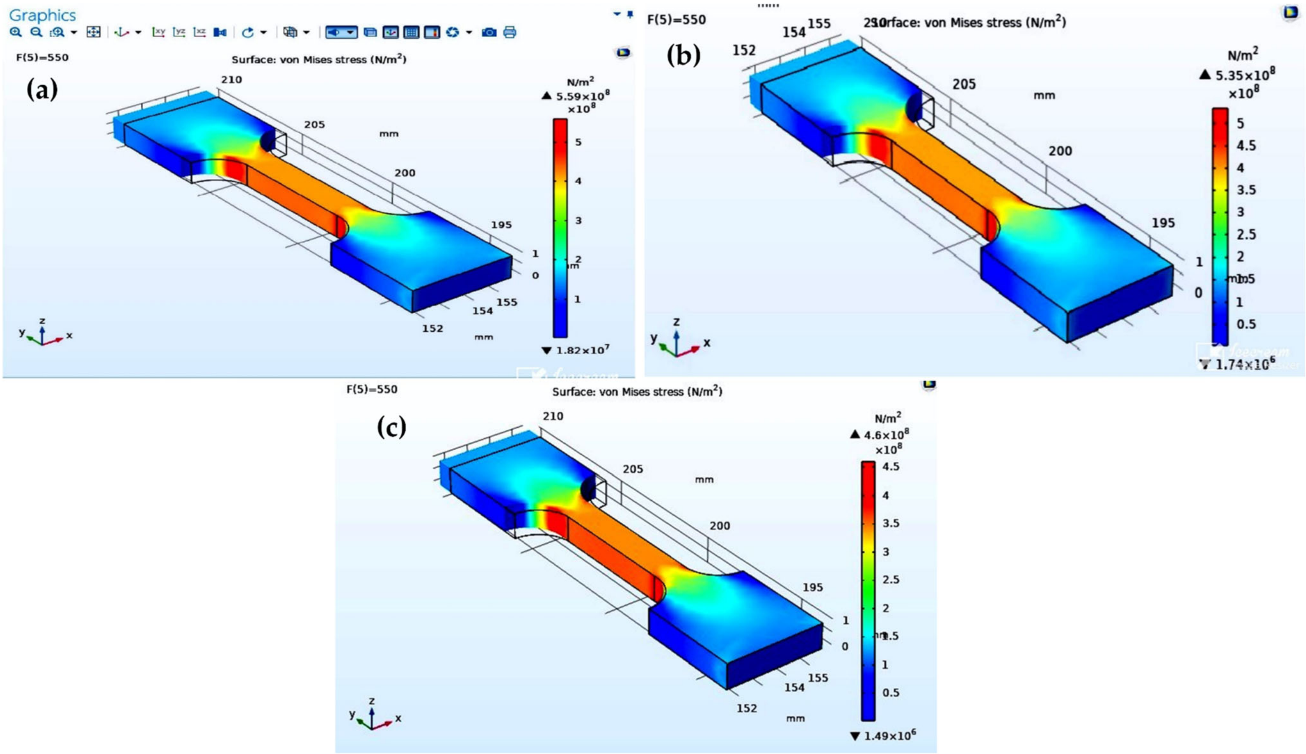

Fig 13 FEA findings for tensile testing simulation outcomes: (a) top, (b) middle, and (c) bottom

mental and numerical data ensures that the FEA model accurately reflects the mechanical behavior of WAAM-fabricated SS309L, thereby confirming its suitability for predicting stress distribution and optimizing WAAM process parameters for enhanced structural performance.

During the validation of the FEA model against experimental data, slight discrepancies of approximately 2-3% were

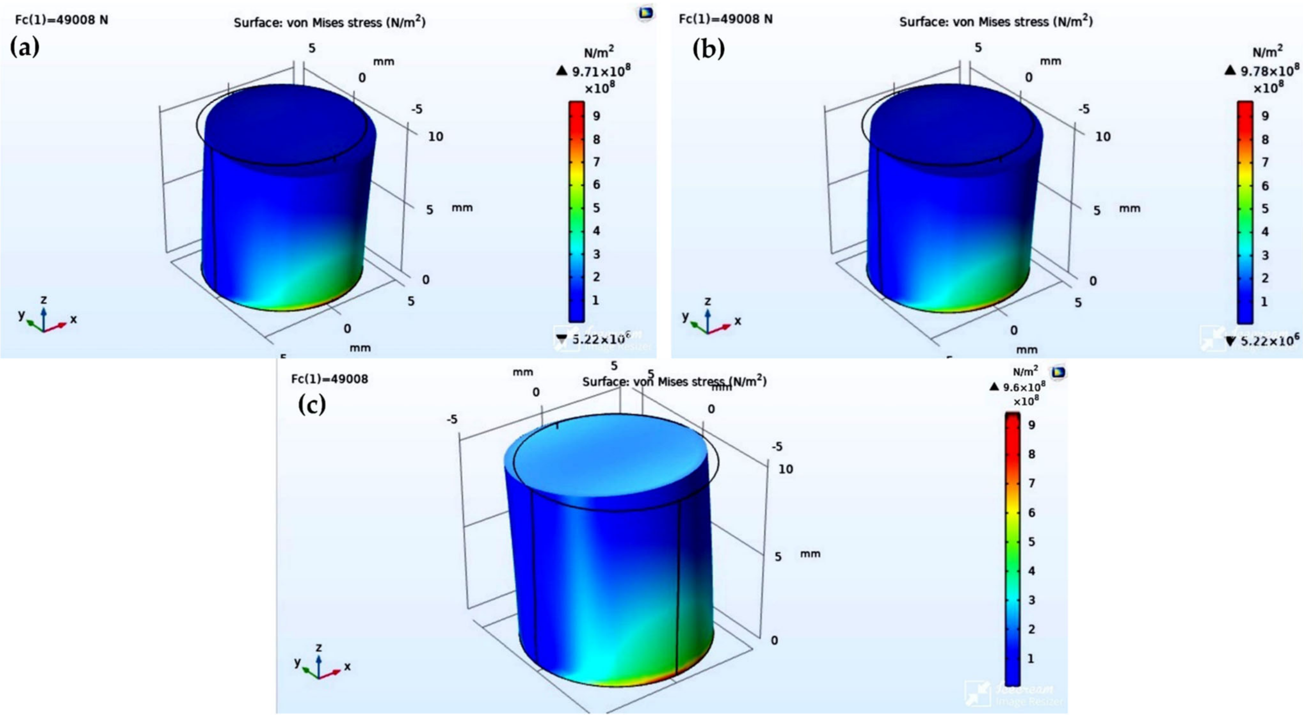

Fig 14 FEA findings for compression testing Simulation outcomes: (a) top, (b) middle, and (c) bottom

Table 5 Comparison of simulation and experimental values for the tensile test

		Maximum stress, MPa	
Sl. no.	WAAM SS309L	Experimental	Simulation
1	Top	561.81	559
2	Middle	545.32	535
3	Bottom	469.73	460

Table 6 Comparison of simulation and experimental values for the Compression Test

		Maximum stress, MPa	
Sl. no.	WAAM SS39L	Experimental	Simulation
1	Top	983.6	971
2	Middle	984.2	978
3	Bottom	978.95	960

observed between the experimental and simulated stress values for both tensile and compressive testing (Tables 5 and 6). These minor variations can be attributed to factors such as microstructural heterogeneity, residual stresses, and minor experimental imperfections. However, the overall trend and mechanical behavior predicted by the FEA model closely match the experimental results. The slight differences are considered acceptable, and they do not undermine the reliability or accuracy of the FEA model in predicting the mechanical performance of WAAM-fabricated SS309L.

3.5.4 SEM Analysis of Tensile Fractured Surfaces for WAAM-Fabricated SS309L. The SEM analysis of the fractured tensile specimens of the WAAM-fabricated SS309L wall provides insights into the fracture mechanisms and ductility variations across the build direction. The micrographs reveal dimpled fracture surfaces, characteristic of ductile failure, where material deformation occurs before fracture due to the nucleation, growth, and coalescence of voids.

In the top section (Fig. 15a), the SEM image displays numerous fine and deep dimples, indicating high plastic deformation before fracture. The smaller dimple size and higher density suggest that the fine-grained microstructure in this region enhances strength, leading to localized plastic deformation. This correlates with the higher tensile strength but lower elongation observed in the experimental results, as the material absorbs significant stress before failure but exhibits limited ductility. The mixed-mode fracture surface is shown for the middle section (Fig. 15b), with moderate dimple size and distribution. Indeed, this implies a compromise between strength and ductility as a stable thermal gradient characterizes the middle region during the WAAM process. Here, in this region, the grain structure is of both columnar and equiaxed grains, leading to balanced fracture behavior in which void formation and coalescence are more uniform. Figure 15(c) shows the bottom section (with larger and deeper dimples, implying higher ductility) than the other two regions. This region has a coarser microstructure and higher ferrite content to permit more considerable plastic deformation before failure. (Ref 58, 59). The higher experimental elongation values confirmed that when subjected to strain energy, the bottom region absorbs more strain energy before fracture and is thus more resistant to brittle failure. Finally, the SEM fracture analysis reveals that the microstructure significantly influences the fracture behavior of WAAM-fabricated SS309L. Finer grains result in the top section fracturing with little plasticity;

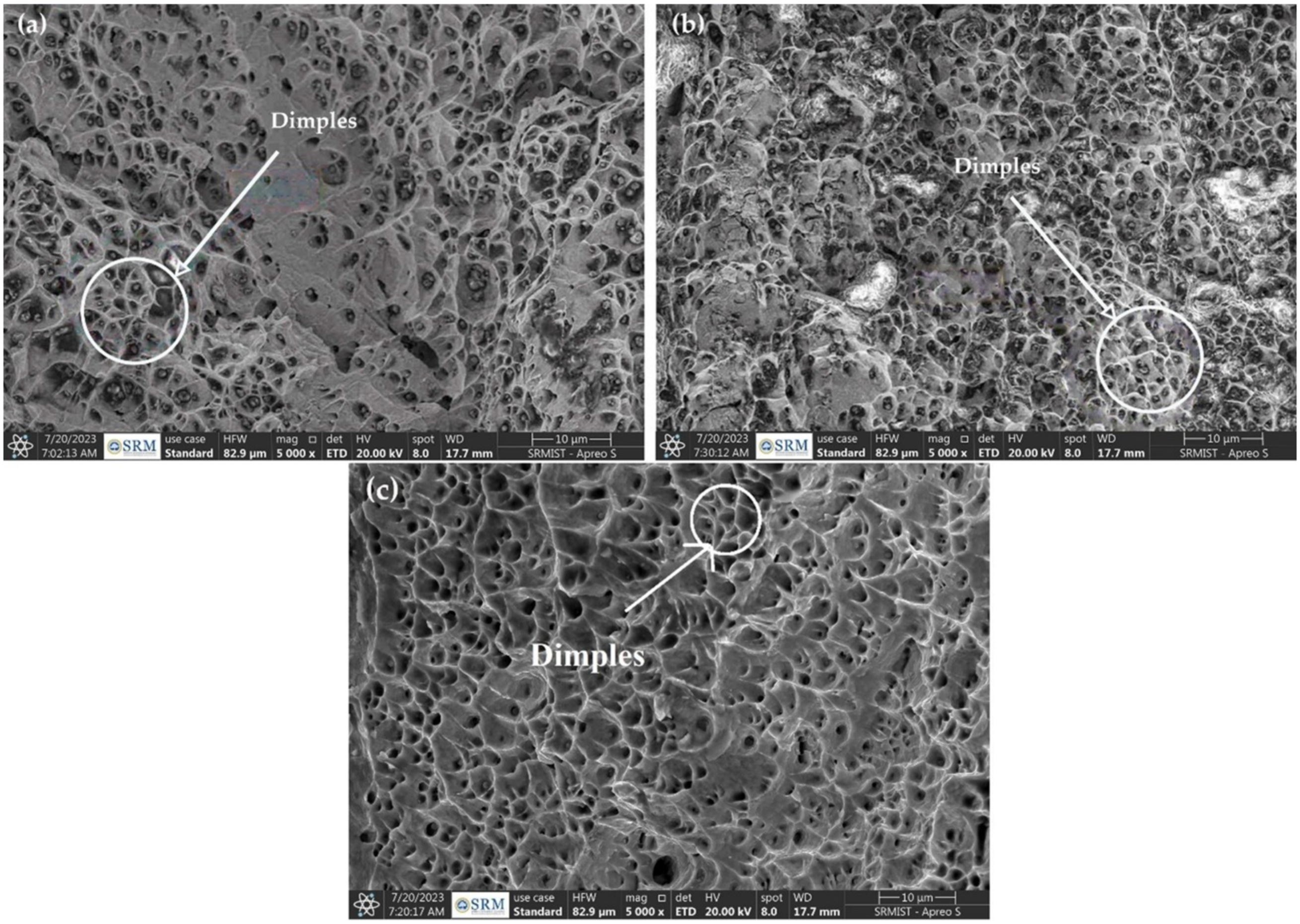

Fig 15 Tensile test fractured surface morphology (a) top (b) middle, and (c) bottom

the middle section exhibits the same balance of ductility response; and the bottom section has the highest ductility and most prominent dimples. The mechanical property trends observed through tensile testing are validated by these findings, which demonstrate that thermal effects and grain evolution play essential roles in WAAM structures.

3.6 Physical Property Analysis of WAAM-Fabricated SS309L: Density and Porosity

The density and porosity measurements of the WAAM-fabricated SS309L were taken in the top, bottom, and middle sections to verify material integrity and structural uniformity. The density values are presented in Table 7, and the porosity percentage at different build heights is presented in Table 8.

The values indicate that it increases gradually from the top to the bottom section. The densities are in ascending order from the bottom section (8.451 g/cm^3), the middle section (7.836 g/cm^3), and again the top section (7.652 g/cm^3). The phenomenon is attributed to the effect of thermal cycles and deposition sequence in the WAAM process. In deposition, the bottom layers are subjected to repeated multiple reheating cycles by the subsequent layers to achieve better material consolidation, minimal void formation, and higher densification. A very slight density variation is introduced due to incomplete fusion and microvoid formation in the top layers, which cool more rapidly.

This observation is supported by the porosity analysis of the sections (Table 8), where the top section has a porosity of 0.0075, the middle section is 0.0076, and the bottom section is 0.0081%. This slight increase in porosity at the bottom section likely results from increased heat input and prolonged thermal exposure, which may have led to gas entrapment and microvoid formation during the solidification process. Compared to all the sections, the porosity levels are very low, suggesting high-quality deposition and fewer defects. Therefore, the density and porosity results indicate that the WAAM SS309L structure remains intact; the densities are higher at the bottom due to thermal effects, and there is slightly higher porosity resulting from gas entrapment. This emphasizes the need to optimize process parameters so that heat input, deposition rate, and cooling mechanism can be controlled to achieve uniform density and minimal porosity in additively manufactured stainless steel components.

Table 7 SS309L density at different positions (g/cm^3)

Sl. no.	Top		Middle		Bottom	
1	Air 0.761 g	7.652 g/cm^3	Air 0.765 g	7.836 g/cm^3	Air 0.853 g	8.451 g/cm^3
2	Water 0.672 g		Water 0.661 g		Water 0.724 g	

Table 8 Porosity in WAAM-Fabricated SS309L

Section	Porosity, %	Standard deviation, %	Error margin, %
Top	0.0075	0.0002	± 0.0002
Middle	0.0076	0.0003	± 0.0003
Bottom	0.0081	0.0004	± 0.0004

4. Conclusions

WAAM-fabricated SS309L stainless steel has been thoroughly analyzed, revealing significant variations in strength, ductility, grain structure, and density along the build direction. This analysis confirms that thermal cycling plays a pivotal role in shaping the microstructure of the fabricated wall, thus influencing its mechanical behavior. The fine-grained microstructure in the top section leads to the highest yield strength (435.63 MPa) and ultimate tensile strength (561.81 MPa). In contrast, the bottom section, with a coarser grain structure and higher ferrite content, exhibits slightly lower tensile strength (469.73 MPa UTS) but improved elongation (45.6%). Compression testing further supports these observations, showing a higher compressive strength in the top section (983.6 MPa) compared to the bottom section (978.95 MPa), illustrating the tradeoff between strength and ductility.

SEM and EBSD analyses reveal grain refinement at the top and coarser columnar grains at the bottom, attributed to prolonged thermal exposure during layer deposition. XRD analysis confirms a higher austenite content in the top region, which enhances strength, while the bottom region exhibits increased ferrite content, improving ductility. Fractography analysis of tensile specimens also highlights that the top section exhibits increased strength with reduced plasticity, as indicated by finned fracture surfaces. In contrast, the bottom section shows larger dimples, signifying enhanced ductility and energy absorption. The numerical simulations, conducted through FEA, align closely with the experimental results for both tensile and compressive tests, validating the accuracy of the model. The FEA simulations confirm that the top section experiences greater stress, while the bottom section demonstrates higher deformation capacity.

Density and porosity measurements revealed the highest density of 8.451 g/cm^3 at the bottom, which is attributed to reheating that facilitated material consolidation. In contrast, the top section exhibited a lower density of 7.652 g/cm^3 due to rapid cooling. The mechanical performance and microstructural stability of WAAM-fabricated SS309L indicate a strong balance, with the top section being suitable for high-strength applications and the bottom section excelling in toughness and ductility. These findings suggest that WAAM can be effectively used to fabricate stainless steel components for advanced engineering applications, offering enhanced structural integrity and performance. The validated FEA model offers a dependable framework for optimizing WAAM processes and predicting mechanical behavior, thereby ensuring efficient and high-performance component manufacturing. Future research can build upon these findings to refine process parameters, reduce defects, and further enhance the structural integrity of parts fabricated through WAAM.

Author Contributions

Tamil Prabakaran S contributed to Experimental Work, Investigation, Materials; Saravanakumar Sengottaiyan contributed to Research Supervision, Methodology, Writing Original Draft; Yogaraj D contributed to Research Administration; and Shaisundaram V S contributed to Optimization and FEA Validation.

Funding

There are no funding sources for this research work.

Data Availability

No new data were used in this study.

Competing interests

The authors declare that they have no competing interests related to this manuscript. The work has not been submitted elsewhere for publication, and all authors have approved the submission. Furthermore, no human participants or animals were involved in this study, ensuring compliance with the ethical standards of research. The research focuses solely on material synthesis, characterization, and computational modeling.

References

1. N. Manikandan and M. Arumugam, Optimizing Cold Metal Transfer-Wire Arc Additive Manufacturing Parameters for Enhanced Mechanical Properties and Microstructure of ER5356 Aluminum Alloy Using Artificial Neural Network and Response Surface Methodology, *J. Mater. Eng. Perform.*, 2025, **34**, p 4853–4872. https://doi.org/10.1007/s11665-024-10403-y
2. Y. Li, S. Yin, G. Zhang, C. Wang, X. Liu, and R. Guan, A Review on Wire Arc Additive Manufacturing of Magnesium Alloys: Wire Preparation, Defects and Properties, *Met. Mater. Int.*, 2024 https://doi.org/10.1007/s12540-024-01724-7
3. M. Srivastava, S. Rathee, A. Tiwari, and M. Dongre, Wire Arc Additive Manufacturing of Metals: A Review on Processes, Materials and Their Behaviour, *Mater. Chem. Phys.*, 2023, **294**, 126988. https://doi.org/10.1016/j.matchemphys.2022.126988
4. M.D.B. Kumar and M. Manikandan, Evaluation of Microstructure, Residual Stress, and Mechanical Properties in Different Planes of Wire + Arc Additive Manufactured Nickel-Based Superalloy, *Met. Mater. Int.*, 2022, **28**(12), p 3033–3056. https://doi.org/10.1007/s12540-022-01185-w
5. A. Sethuraman, E. Vijayaragavan, T. Lakshmanan, T. Geethapriyan, and I.A. Palani, Optimization and Finite Element Analysis Simulation

on Mechanical Behavior of Wire Arc Additive Manufacturing for SS316L Using Response Surface Methodology, *J. Mater. Eng. Perform.*, 2025 https://doi.org/10.1007/s11665-025-10776-8

6. T. Wang, J. Tang, D. Guo, J. Lei, L. Li, and H. Han, Effect of Solution and Double-Stage Aging Treatment on the Microstructure and Mechanical Properties of CMT-WAAM Inconel625 Structural Components, *Met. Mater. Int.*, 2024, **30**(10), p 2916–2924. https://doi.org/10.1007/s12540-024-01686-w
7. E. Tenuta, A. Nycz, M. Noakes, S. Simunovic, and M.H.A. Piro, Material Properties and Mechanical Behaviour of Functionally Graded Steel Produced by Wire-Arc Additive Manufacturing, *Addit. Manuf.*, 2021, **46**, p 1–36
8. W.J. Oh, C.M. Lee, and D.H. Kim, Prediction of Deposition Bead Geometry in Wire Arc Additive Manufacturing Using Machine Learning, *J. Mater. Res. Technol.*, 2022, **20**, p 4283–4296
9. V. Monfared, S. Ramakrishna, N. Nasajpour-Esfahani, D. Toghraie, M. Hekmatifar, and S. Rahmati, Science and Technology of Additive Manufacturing Progress: Processes, Materials, and Applications, *Met. Mater. Int.*, 2023, **29**(12), p 3442–3470. https://doi.org/10.1007/s12540-023-01467-x
10. V.T. Le, D.S. Mai, T.K. Doan, and H. Paris, Wire and Arc Additive Manufacturing of 308L Stainless Steel Components: Optimization of Processing Parameters and Material Properties, *Eng. Sci. Technol. Int. J.*, 2021, **24**(4), p 1015–1026. https://doi.org/10.1016/j.jestch.2021.01.009
11. Z. Lyu, Y.S. Sato, S. Tokita, Y. Zhao, J. Jia, and A. Wu, Homogenization of Microstructure and Mechanical Properties of Wire Arc Additive Manufactured Martensitic Stainless Steel Through Optimization of Post-Process Heat Treatment, *J. Mater. Res. Technol.*, 2022, **21**, p 2682–2692. https://doi.org/10.1016/j.jmrt.2022.10.077
12. P.N. Bellamkonda, M. Dwivedy, M. Sudersanan, and B. Visvalingam, Influence of Welding Processes on the Microstructure and Mechanical Properties of Duplex Stainless Steel Parts Fabricated by Wire Arc Additive Manufacturing, *Met. Mater. Int.*, 2025, **31**(2), p 368–391. https://doi.org/10.1007/s12540-024-01753-2
13. J. Chen, H. Wei, K. Bao, X. Zhang, Y. Cao, Y. Peng, J. Kong, and K. Wang, Dynamic Mechanical Properties of 316L Stainless Steel Fabricated by an Additive Manufacturing Process, *J. Mater. Res. Technol.*, 2021, **11**, p 170–179. https://doi.org/10.1016/j.jmrt.2020.12.097
14. C. Rakesh, P. Heet, V. Jay, and P. Vivek, Parametric Study and Investigations of Bead Geometries of GMAW-Based Wire-Arc Additive Manufacturing of 316L Stainless Steels, *Metals (Basel).*, 2022, **12**, 1232
15. L. Zhao, J. Zhang, J. Yang, J. Hou, J. Li, and J. Lin, Microstructure and Mechanical Properties of 316L Stainless Steel Manufactured by Multi-laser Selective Laser Melting (SLM), *Mater. Sci. Eng. A*, 2024, **913**, 147053. https://doi.org/10.1016/j.msea.2024.147053
16. S.V. Motghare, K.M. Ashtankar, and N.K. Lautre, Experimental Investigation of Electrochemical and Mechanical Properties of Stainless Steel 309L at Different Built Orientation by Cold Metal Transfer Assisted Wire Arc Additive Manufacturing, *Mater. Today Commun.*, 2024, **39**, 109382. https://doi.org/10.1016/j.mtcomm.2024.109382
17. S. Prabhakaran, B. Vinod, S. Suresh, and K. Asokkumar, Implementation of Automated Gas Tungsten Arc Welding (AGTAW) for Stainless Steel 309L Applications, *Int. J. Aquat. Sci.*, 2021, **12**(02), p 2021
18. C. Wichan and S. Loeshpahn, Effect of Filler Alloy on Microstructure, Mechanical and Corrosion Behaviour of Dissimilar Weldment Between AISI 201 Stainless Steel and Low Carbon Steel Sheets Produced by a Gas Tungsten Arc Welding, *Adv. Mater. Res.*, 2012 https://doi.org/10.4028/www.scientific.net/AMR.581-582.808
19. M. Gao, C. Chen, S. Mei, L. Wang, and X. Zeng, Parameter Optimization and Mechanism of Laser-Arc Hybrid Welding of Dissimilar Al Alloy and Stainless Steel, *Int. J. Adv. Manuf. Technol.*, 2014, **74**(1–4), p 199–208
20. A. Thirugnanasambandam, M.K. Subramaniyan, A. Gobiraman, and V. Elumalai, Wire plus Arc Additive Manufacturing of Stainless Steel Wall for Predicting Parametric Influences on Strength: Experimentation and Finite-Element Analysis Approach, *Proc. Inst. Mech. Eng. Part. E J Process. Mech. Eng.*, 2024 https://doi.org/10.1177/09544089241241900
21. D. Shetty, V. Vijayan, and K. Natesan, An Experimental Study on Wire Arc Additive Manufacturing (WAAM) of 308L Stainless Steel and Its Chemical Dissolution, *Weld. Int.*, 2025, **39**(2), p 134–140. https://doi.org/10.1080/09507116.2024.2410451
22. V.T. Le and D.S. Mai, Microstructural and Mechanical Characteristics of 308L Stainless Steel Manufactured by Gas Metal Arc Welding-Based Additive Manufacturing, *Mater. Lett.*, 2020, **271**, 127791. https://doi.org/10.1016/j.matlet.2020.127791
23. Y. Ke and J. Xiong, Microstructure and Mechanical Properties of Double-Wire Feed GTA Additive Manufactured 308L Stainless Steel, *Rapid Prototyp. J.*, 2020, **26**(9), p 1503–1513
24. R. Chaudhari, S. Khanna, J. Vora, and V. Patel, Experimental Investigations on Microstructure and Mechanical Properties of Wall Structure of SS309L Using Wire-Arc Additive Manufacturing, *J. Adv. Join. Process.*, 2023, **2024**(9), p 100172. https://doi.org/10.1016/j.jajp.2023.100172
25. J. Sivakumar, J. Lakshmipathy, and E. Uthirapathi, An investigation on Surface Integrity and Microstructure Behaviour of AISI 304 Stainless Steel Machined by Die Sinking EDM, *Metall. Res. Technol.*, 2024, **121**(5), p 511. https://doi.org/10.1051/metal/2024065
26. U. Elaiyarasan, C. Nandakumar, and T. Arunkumar, Experimental Study on Parametric Effect of Wire Electric Discharge Machining of Titanium Grade 2 Alloy Using Cryogenic Treated Wire, *J. Mater. Eng. Perform.*, 2024 https://doi.org/10.1007/s11665-024-09976-5
27. U. Elaiyarasan, P. Baranitharan, V. Satheeshkumar, C. Senthilkumar, and B. Vinod, Wear Behaviour and Coating Performance of WC–Cu Composite Electrodes on ZE41A Magnesium Alloy Using Electrospark Deposition, *Can. Metall. Q.*, 2024, **4433**, p 1–14. https://doi.org/10.1080/00084433.2024.2437218
28. U. Elaiyarasan, P. Baranitharan, V. Satheeshkumar, C. Senthilkumar, and T. Arunkumar, Evaluation on Tribological Performance of Ti-6Al-4V Alloy Modified Using Powder Composite Electrode-Assisted Electrical Discharge Coating, *JOM*, 2024, **77**(4), p 1834–1843. https://doi.org/10.1007/s11837-024-07070-8
29. T. Elangovan, J. Ajith, G.V. Hariharan, S. Dinesh Kumar, M. Manickam, and U. Elaiyarasan, Surface Integrity and Microstructure Analysis of the AZ31B Magnesium Alloy Machined by Sustainable EDM with a B4C-Enriched Bio-Dielectric Fluid, *Can. Metall. Q.*, 2025, **4433**, p 1–11. https://doi.org/10.1080/00084433.2025.2471613
30. U. Elaiyarasan, V. Satheeshkumar, C. Senthilkumar, and T. Arunkumar, Enhancing Microhardness and Surface Integrity of Ti–6Al–4V Alloy Using WC–Cu Composite Electrode Aided Electrical Discharge Coating, *J. Adhes. Sci. Technol.Adhes. Sci. Technol.*, 2024, **39**(4), p 596–614. https://doi.org/10.1080/01694243.2024.2415350
31. G.I. Khidhir, S.A. Baban, and Brazilian Metallurgical, Materials and Mining Association, Efficiency of Dissimilar Friction Welded 1045 Medium Carbon Steel and 316L Austenitic Stainless Steel Joints, *J. Mater. Res. Technol.*, 2019, **8**(2), p 1926–1932
32. D. Van Thuc, D. Van Luu, P. Hoang Cuong, Q. Tien Ha, T. Dinh, and T. Van Dinh, Influence of WAAM Process Parameters on Morphology of Beads When Coating High-Temperature Stainless Steels SS309L on Low Carbon Steel Plates, *Irjaes. Com*, 2023, **8**(2), p 183–186
33. S. Sengottaiyan, S. Sathiyamurthy, and G. Selvakumar, Influence of Treatment and Fly Ash Fillers on the Mechanical and Tribological Properties of Banana Fiber Epoxy Composites: Experimental and ANN- RSM Modeling, *Compos. Interfaces*, 2025, **32**(7), p 953–985. https://doi.org/10.1080/09276440.2024.2448879
34. S. Saravanakumar, S. Sathiyamurthy, N. Ananthi, and P. Devi, Optimization of Drilling Characteristics of Al2O3 and Boiled Eggshell Filler-Added Hybrid Bio Composite from Agriculture Residue, *Biomass Convers. Biorefin.*, 2024, **14**(23), p 29321–29335. https://doi.org/10.1007/s13399-023-04572-4
35. T. Kurzynowski, K. Gruber, W. Stopyra, B. Kuźnicka, and E. Chlebus, Correlation between Process Parameters, Microstructure and Properties of 316 L Stainless Steel Processed by Selective Laser Melting, *Mater. Sci. Eng. A*, 2017, **2018**(718), p 64–73
36. L. Wang, J. Hu, E. Guo, Y. Li, H. Kang, and Y. Feng, Microstructure and Mechanical Properties of Thick-Walled WE43A Alloy Fabricated by Wire Arc Additive Manufacturing, *J. Mater. Eng. Perform.*, 2024 https://doi.org/10.1007/s11665-024-10270-7
37. O. Basil Quent, C.C. Nwobi-Okoye, P.U. Ochieze, and I.A. Ochieze, Microstructural and Properties Evaluation of A356 Alloy/Cow Horn Particulate Composites Produced by Spark Plasma Sintering, *J. Chinese Adv. Mater. Soc.*, 2018, **6**(1), p 30–43. https://doi.org/10.1080/22243682.2017.1387604
38. S. Joy and J.K. Antony, Design and Simulation of a Micro Hotplate Using COMSOL Multiphysics for MEMS Based Gas Sensor, *Fifth*

International Conference on Advances in Computing and Communications (ICACC), 2015, **2015**, p 465–468

39. A. Jafari, P. Broumand, M. Vahab, and N. Khalili, An EXtended Finite Element Method Implementation in COMSOL Multiphysics: Solid Mechanics, *Finite Elem. Anal. Des.*, 2022, **202**, 103707. https://doi.org/10.1016/j.finel.2021.103707
40. S. Sathiyamurthy, S. Saravanakumar, N. Ananthi, and P. Devi, Optimization of Fiber Length and Filler Content for Improving the Mechanical Behaviour of *Musa acuminate* Fiber-Reinforced Epoxy Composite Using Response Surface Methodology, *J. Ceram. Process. Res.*, 2023, **24**(4), p 683–692
41. S. Sengottaiyan, S. Subbarayan, R. Natarajan, and V. Gurunathan, Enhancing Mechanical, Degradation, and Tribological Properties of Biocomposites via Treatment and Alumina Content, *J. Reinf. Plast. Compos.*, 2025 https://doi.org/10.1177/07316844251321664
42. U. Elaiyarasan, N. Ananthi, and S. Sathiyamurthy, Prediction and Parametric Effect of Electrical Discharge Layering of AZ31B Magnesium Alloy Using Response Surface Methodology-Assisted Artificial Neural Network, *Bull. Mater. Sci.*, 2024 https://doi.org/10.1007/s12034-024-03184-6
43. S. Saravanakumar, S. Sathiyamurthy, P. Pathmanaban, and P. Devi, Integrating Machine Learning and Response Surface Methodology for Analyzing Anisotropic Mechanical Properties of Biocomposites, *Compos. Interfaces*, 2024, **31**(1), p 1–28. https://doi.org/10.1080/09276440.2023.2260239
44. S. Sengottaiyan, S. Subbarayan, V. Viswanathan, and P. Pugazhendi, Optimized Machine Learning with Hyperparameter Tuning and Response Surface Methodology for Predicting Tribological Performance in Bio-composite Materials, *Polym. Compos.*, 2024, **45**(10), p 9421–9439. https://doi.org/10.1002/pc.28418
45. S. Sathiyamurthy, S. Saravanakumar, and V. Vinoth, Enhancing Tribological Performance of Hybrid Fiber-Reinforced Composites through Machine Learning and Response Surface Methodology. *J. Reinf. Plast. Compos.*, 2024. https://doi.org/10.1177/0731684424125642
46. S. Saravanakumar, S. Sathiyamurthy, and V. Vinoth, Enhancing Machining Accuracy of Banana Fiber-Reinforced Composites with Ensemble Machine Learning, *Meas. J. Int. Meas. Confed.*, 2024, **235**(March), p 114912. https://doi.org/10.1016/j.measurement.2024.114912
47. U. Elaiyarasan, V. Satheeshkumar, and C. Senthilkumar, Parametric Effect on Electrical Discharge Treatment of Magnesium Alloy with Powder Composite Electrode, *SN Appl. Sci.*, 2020, **2**(3), p 1–10. https://doi.org/10.1007/s42452-020-2184-7
48. V. Vinoth, S. Sathiyamurthy, S. Saravanakumar, and R. Senthilkumar, Integrating Response Surface Methodology and Machine Learning for Analyzing the Unconventional Machining Properties of Hybrid Fiber-Reinforced Composites, *Polym. Compos.*, 2024, **45**(7), p 6077–6092
49. S. Sengottaiyan, V.S. Shaisundaram, M.S. Basha, B. Deepanraj, and N. Senthilkumar, Effect of Duplex and Austenite Stainless Steel Fillers on Mechanical, Microstructural, and Corrosion Characteristics of Dissimilar Welds Using Cold Metal Transfer Welding, *Results Eng.*, 2025 https://doi.org/10.1016/j.rineng.2025.104818
50. S. Sengottaiyan, S. Subbarayan, R. Natarajan, and V. Gurunathan, Synergistic Effects of NaOH Treatment and Ceramic Fillers on the Mechanical and Tribological Behavior of Roselle Fiber-Reinforced Epoxy Composites, *Fibers Polym.*, 2025, **26**(5), p 2077–2095. https://doi.org/10.1007/s12221-025-00922-3
51. G. Periyappillai, S. Subbarayan, and S. Sengottaiyan, Advanced Ensemble Machine Learning Prediction to Enhance the Accuracy of Abrasive Waterjet Machining for Biocomposites, *Mater. Chem. Phys.*, 2025, **333**, 130175. https://doi.org/10.1016/j.matchemphys.2024.130175
52. G. Periyappillai, S. Sathiyamurthy, S. Saravanakumar, and The Korean Fiber Society, Optimized Machine Learning Prediction and RSM Optimization of Mechanical Properties in Boiled Eggshell Filler-Added Biocomposites, *Fibers Polym.*, 2024, **25**(8), p 3115–3133. https://doi.org/10.1007/s12221-024-00638-w
53. P. Long, D. Wen, J. Min, Z. Zheng, J. Li, and Y. Liu, Microstructure Evolution and Mechanical Properties of a Wire-Arc Additive Manufactured Austenitic Stainless Steel: Effect of Processing Parameter, *Materials*, 2021 https://doi.org/10.3390/ma14071681
54. Z. Du, Y. Wang, J. Chen, Q. Zhang, C. Li, Y. Jiang, Y. Pu, and X. Wang, Effect of Additive Manufacturing Thickness on Microstructure and Properties of DG09 Welding Wire Wear-Resistant Layer, *J. Phys. Conf. Ser.*, 2023 https://doi.org/10.1088/1742-6596/2549/1/012008
55. J.S. Kumar, M. Qasim, and S. Pushpendra, Microstructural and Mechanical Properties Analysis of SS 316L Structure Fabricated Using CMT- Wire Arc Additive Manufacturing, *J. Adhes. Sci. Technol.Adhes. Sci. Technol.*, 2024 https://doi.org/10.1080/01694243.2024.2399115
56. N. Arivazhagan, M. Manikandan, and G. Kumar, Heliyon Pulsed Directed Energy Deposition-Arc Technology for Depositing Stainless Steel 309L: Microstructural, Elements Distribution, and Mechanical Characteristics, *Heliyon*, 2024, **10**(15), p e35279. https://doi.org/10.1016/j.heliyon.2024.e35279
57. C. Chen, W. Du, H. Zhang, and X. Zhao, Improvement of Microstructure and Mechanical Properties of Stainless Steel TIG Based Wire Arc Additive Manufacturing by Using AC/DC Mix Current Waveform, *J. Mater. Res. Technol.*, 2023, **23**, p 4355–4366. https://doi.org/10.1016/j.jmrt.2023.02.093
58. V. Amiri and H. Naffakh-Moosavy, Wire Arc Additive Manufacturing of Functionally Graded Carbon Steel - Stainless Steel 316L - Inconel 625: Microstructural Characterization and Mechanical Behavior, *J. Adv. Join. Process.*, 2024, **9**(1), p 100194. https://doi.org/10.1016/j.jajp.2024.100194
59. X. Chen, J. Li, X. Cheng, B. He, H. Wang, and Z. Huang, Microstructure and Mechanical Properties of the Austenitic Stainless Steel 316L Fabricated by Gas Metal Arc Additive Manufacturing, *Mater. Sci. Eng. A*, 2017, **703**, p 567–577